

ON THE INTERPRETATION OF THE PIECEWISE SMOOTH VISIBLE-INVISIBLE TWO-FOLD SINGULARITY IN \mathbb{R}^3 USING REGULARIZATION AND BLOWUP

K. ULDALL KRISTIANSEN AND S. J. HOGAN*

Abstract.

Using geometric singular perturbation theory and the blowup method in the formulation of Krupa and Szmolyan, we show that under generic conditions the Sotomayor and Teixeira regularization of the piecewise smooth visible-invisible two-fold possesses a limit cycle attracting a large set of initial conditions. This in turn offers a deterministic interpretation of the forward ambiguity associated with the piecewise smooth two-fold since the regularization selects a distinguished orbit among all the candidates passing through the two-fold. The result is independent of the monotonic regularization function $\phi \in C^k$, $1 \leq k < \infty$.

Key words. Piecewise smooth systems, blowup, geometric singular perturbation theory, sliding bifurcations, canards, two-fold.

AMS subject classifications. 37G10, 34E15, 37M99

1. Introduction. A piecewise smooth (PWS) dynamical system [11, 20] consists of a finite set of ordinary differential equations

$$\dot{\mathbf{x}} = f_i(\mathbf{x}), \quad \mathbf{x} \in R_i \subset \mathbb{R}^n \quad (1.1)$$

where the smooth vector fields f_i , defined on disjoint open regions R_i , are smoothly extendable to the closure of R_i . The regions R_i are separated by an $(n - 1)$ -dimensional set Σ called the *switching boundary*, which consists of finitely many smooth manifolds intersecting transversely. The union of Σ and all R_i covers the whole state space $D \subseteq \mathbb{R}^n$. In this paper, we consider $n = 3$, building upon previous work in [15].

When the normal components of the vector fields either side of Σ are in the *same* direction, the gradient of a trajectory is discontinuous, leading to Carathéodory solutions [6]. In this case, the dynamics is described as *crossing* or *sewing*. But when the normal components of the vector fields either side of Σ are in the *opposite* direction, a vector field *on* Σ needs to be defined. The precise choice is not unique and crucially depends on the nature of the problem under consideration. A popular, and in many cases physically realistic, choice is to adopt the Filippov convention [11], where a *sliding* vector field is defined on Σ . In this case, the dynamics is described as *sliding*. *Stable (unstable)* sliding occurs when the flow on both sides of Σ is directed towards (away from) Σ .

A sliding bifurcation occurs where the relative direction of the normal component of vector fields on either side of Σ is reversed under parameter variation. Crossing and sliding interchange, leading to fundamentally different dynamics. The fundamental geometric objects involved in sliding bifurcations are: the fold, the cusp and the two-fold. The two-fold is the singularity at the intersection of two folds, either of which may be visible or invisible. This gives rise to three different types of two-fold: visible-visible (or just visible), visible-invisible, or invisible-invisible (or just invisible). In \mathbb{R}^3 , the switching boundary Σ is topologically equivalent to a plane. Then around the two-fold singularity, Σ is divided into four regions: up and down crossing and stable and unstable sliding.

It has been shown [7] that two-folds in \mathbb{R}^3 contain dynamics that is very similar to canards [1]. Within Σ , trajectories of the sliding vector field, which start in the stable sliding region, pass through the two-fold and then may enter the unstable sliding region. The existence of (singular) canards in PWS systems is associated with forward non-uniqueness. So how do we continue orbits forward in time? Are there orbits that are distinguished among all the candidates?

Previous work has attempted to resolve this question. In [21], the planar visible two-fold was considered. The ambiguity of forward evolution was removed using separate small perturbations: hysteresis, time-delay and noise. In each case, a probabilistic notion of forward evolution close to the two-fold was developed. In the limit as the perturbation tended to zero, almost all orbits or sample paths followed one of the visible tangencies. Thus the possibility of evolution through the two-fold singularity into the escaping region for

*K. Uldall Kristiansen: Department of Applied Mathematics and Computer Science, Technical University of Denmark, 2800 Kgs. Lyngby, DK. S. J. Hogan: Department of Engineering Mathematics, University of Bristol, Bristol BS8 1UB, United Kingdom.

a nonzero length of time could be excluded, similar to other results for non-differentiable systems in the zero-noise limit. The author also made the point that the regularization of two-folds may turn out to be futile in the absence of further physical (or biological) information about the problem.

In [5], all three two-folds in \mathbb{R}^3 were considered. For the invisible two-fold, the authors asserted that forward evolution through the singularity into the region of unstable sliding *is* possible. Then after a finite time, evolution away from the unstable sliding region leads to a return mechanism to the stable sliding region and a subsequent forward evolution through the singularity, leading to what they called “nondeterministic chaos”. No such claims were made for either the visible or the visible-invisible two-fold, in line with the conclusions in [21].

The aim of the current paper is to demonstrate a deterministic notion for the visible-invisible two-fold. We illustrate our approach in Fig. 1.1. The presence of forward nonuniqueness is a failure of the PWS system to provide a complete description of the dynamics. This breaks the green arrow in the lower row of the figure. Nevertheless, it is well-known that lifting the nonsmooth system to a smooth one, through the process of Sotomayor-Teixeira regularization [22], we gain uniqueness of solutions. In this paper we capture the limiting dynamics, as the regularized system approaches the nonsmooth version, by applying geometric singular perturbation theory and blowup [17, 19]. This framework provides a route (following the red arrows) to extend PWS models and understand the dynamical role of the paradoxical situations.

In [15] the present authors regularized two-folds in \mathbb{R}^3 , and found canards for $\epsilon \ll 1$, where ϵ is a parameter that measures how close the regularized system is to the PWS system. In agreement with [7], the visible-invisible two-fold was shown to bear many similarities with the folded node in classical slow-fast theory [23, 25]. In particular, among a whole sector of (singular) canards of the PWS system, we obtained one *weak* canard for $\epsilon \ll 1$ (within fixed copies of extended slow manifolds), and demonstrated the existence of so-called secondary canards.

In [16], the visible-invisible two-fold in \mathbb{R}^2 was shown, following the approach illustrated in Fig. 1.1, to be closely related to the canard explosion phenomena known from the van der Pol system [18]. This provided an interpretation of the associated PWS system. Here we apply the same approach to provide an interpretation of the visible-invisible two-fold in \mathbb{R}^3 . We consider a generic case in which the forward orbit of the two-fold on the visible side, as just one of the many forward orbits through the two-fold, returns to the two-fold. This gives rise to a closed cycle which we call a *closed PWS singular cycle*; see Fig. 4.1. We then show the following:

- The existence of a limit cycle of the regularization which converges to the closed PWS singular cycle as $\epsilon \rightarrow 0$ (see Theorem 4.1 and the precise assumptions in section 4). This limit cycle attracts almost every orbit passing near the two-fold. The exceptional set is extremely small with respect to the regularization parameter (presumably exponentially small).
- The result is (qualitatively) independent of the Sotomayor and Teixeira regularization functions we consider.
- As a corollary, upon regularization, almost all initial conditions within the stable sliding region leave the two-fold by following the forward orbit associated with the visible fold. See Proposition 5.5 and Remark 5.6. This orbit is therefore distinguished among all the forward candidates through the two-fold.

Our setting is similar to the situation considered in [4] in association with the classical folded node. Our analysis and results further strengthen the connection between PWS bifurcations and slow-fast phenomena.

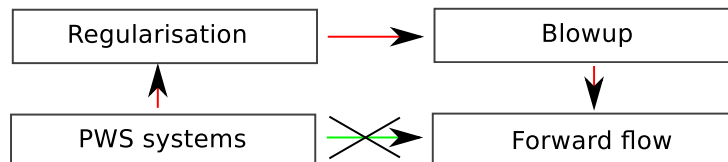


FIGURE 1.1. *Our approach*

Our paper is structured as follows. Sections 2 and 3 are devoted to background. In section 2, for example, we present the basic PWS theory and results from [15] on the normalized equations of motion for the visible-invisible two-fold. Following, Sotomayor and Teixeira [22], we then present the regularization of

our PWS system in section 3. We state our hypothesis and present our main result (Theorem 4.1) in section 4. In section 5 we outline our approach. We identify a closed singular cycle of the regularization and define a return mapping \mathcal{P}_ϵ which we decompose as a global mapping \mathcal{G}_ϵ and a local one \mathcal{L}_ϵ . Properties of \mathcal{L}_ϵ in Proposition 5.5 allow us to prove Theorem 4.1 in section 6. In section 7 we illustrate our main results using numerical computations. Here we also investigate the role of a non-degeneracy condition. We conclude the paper in section 8.

2. PWS system. In this section, we introduce our notation, describe the key concepts from PWS theory and recall results from [15]. Let $\mathbf{x} = (x, y, z) \in \mathbb{R}^3$ and consider an open set \mathcal{U} and a smooth function $f = f(\mathbf{x})$ having 0 as a regular value. Then $\Sigma \subset \mathcal{U}$ defined by $\Sigma = f^{-1}(0)$ is a smooth $2D$ manifold. The manifold Σ will be our *switching manifold*. It separates the set $\Sigma_+ = \{\mathbf{x} \in \mathcal{U} | f(\mathbf{x}) > 0\}$ from the set $\Sigma_- = \{\mathbf{x} | f(\mathbf{x}) < 0\}$. We introduce local coordinates so that $f(\mathbf{x}) = y$ and $\Sigma = \{\mathbf{x} \in \mathcal{U} | y = 0\}$.

We consider two smooth vector-fields X^+ and X^- that are smooth on $\bar{\Sigma}_+$ and $\bar{\Sigma}_-$, respectively, and define the PWS vector-field $X = (X^-, X^+)$ by

$$X(\mathbf{x}) = \begin{cases} X^-(\mathbf{x}) & \text{for } \mathbf{x} \in \Sigma_- \\ X^+(\mathbf{x}) & \text{for } \mathbf{x} \in \Sigma_+ \end{cases} \quad (2.1)$$

Then Σ is divided into two types of region: crossing and sliding:

- $\Sigma_{cr} \subset \Sigma$ is the *crossing region*, where

$$(X^+f(x, 0, z))(X^-f(x, 0, z)) = X_2^+(x, 0, z)X_2^-(x, 0, z) > 0.$$

- $\Sigma_{sl} \subset \Sigma$ is the *sliding region*, where

$$(X^+f(x, 0, z))(X^-f(x, 0, z)) = X_2^+(x, 0, z)X_2^-(x, 0, z) < 0.$$

Here $X^\pm f = \nabla f \cdot X^\pm$ denotes the Lie-derivative of f along X^\pm . Since $f(\mathbf{x}) = y$ in our coordinates we have simply that $X^\pm f = X_2^\pm$. On Σ_{sl} we follow the Filippov convention [11] and define the sliding vector-field $X_{sl}(\mathbf{x})$ as the convex combination of X^+ and X^-

$$X_{sl}(\mathbf{x}) = \sigma X^+(\mathbf{x}) + (1 - \sigma)X^-(\mathbf{x}), \quad (2.2)$$

where $\sigma \in (0, 1)$ is defined so that the vector-field $X_{sl}(\mathbf{x})$ is tangent to Σ_{sl} :

$$\sigma = \frac{X^-f(x, 0, z)}{X^-f(x, 0, z) - X^+f(x, 0, z)}.$$

An orbit of a PWS system can be made up of a concatenation of arcs from Σ and Σ_\pm . The boundaries of Σ_{sl} and Σ_{cr} where $X^+f = X_2^+ = 0$ or $X^-f = X_2^- = 0$ are singularities called *tangencies*. In what follows, we define two different types of generic tangencies: the fold and the two-fold.

DEFINITION 2.1. *A point $q \in \Sigma$ is a fold singularity if*

$$X^+f(q) = 0, \quad X^+(X^+f)(q) \neq 0, \quad \text{and} \quad X^-f(q) \neq 0, \quad (2.3)$$

or

$$X^-f(q) = 0, \quad X^-(X^-f)(q) \neq 0, \quad \text{and} \quad X^+f(q) \neq 0. \quad (2.4)$$

A point $q \in \Sigma$ is a two-fold singularity if both $X^+f(q) = 0$ and $X^-f(q) = 0$, as well as $X^+(X^+f)(q) \neq 0$ and $X^-(X^-f)(q) \neq 0$ and if the vectors $X^+(q)$ and $X^-(q)$ are not parallel.

We have

PROPOSITION 2.2. [15, Proposition 2.2] *A two-fold singularity q is the transversal intersection of two lines l^+ and l^- of fold singularities satisfying (2.3) and (2.4) respectively.*

For a fold, it is important to distinguish between the *visible* and *invisible* cases.

DEFINITION 2.3. [12, Definition 2.1] *A fold singularity q with $X^+f(q) = 0$ or $X^-f(q) = 0$ is visible if*

$$X^+(X^+f)(q) > 0 \quad \text{or} \quad X^-(X^-f)(q) < 0, \quad \text{respectively,}$$

and invisible if

$$X^+(X^+f)(q) < 0 \quad \text{or} \quad X^-(X^-f)(q) > 0, \quad \text{respectively.}$$

Similarly we say the following:

DEFINITION 2.4. [12, Definition 2.3] *The two-fold singularity q is*

- visible if the fold lines l^+ and l^- are both visible;
- visible-invisible if l^+ (l^-) is visible and l^- (l^+) is invisible;
- invisible if l^+ and l^- are both invisible.

2.1. The visible-invisible two-fold. In this paper we focus our attention on the visible-invisible case, taking, without loss of generality, l^+ to be visible and l^- to be invisible. Following [15, Proposition 3.1], this case is locally described by the following set of *normalized equations*:

$$\begin{aligned} \dot{x} &= |\beta|^{-1}c + O(x + y + z), \\ \dot{y} &= ay + bz + \mathcal{O}((y + z)(x + y + z)), \\ \dot{z} &= 1 + O(x + y + z), \end{aligned} \tag{2.5}$$

for $y > 0$ and

$$\begin{aligned} \dot{x} &= -1 + \mathcal{O}(x + y + z), \\ \dot{y} &= \alpha y - |\beta|x + \mathcal{O}((x + y)(x + y + z)), \\ \dot{z} &= b^{-1}\gamma + O(x + y + z), \end{aligned} \tag{2.6}$$

for $y < 0$, where

$$\beta < 0, \quad b > 0, \quad c - \gamma \geq 0. \tag{2.7}$$

In this paper, we shall suppose the following:

$$c + \gamma > \sqrt{(c - \gamma)^2 + 4b\beta}, \quad (c - \gamma)^2 + 4b\beta > 0. \tag{2.8}$$

This condition gives rise to the sliding flow illustrated in Fig. 2.2; see Proposition 2.5. In (2.5) and (2.6), the fold lines

$$\begin{aligned} l^+ &: y = 0 = z, \\ l^- &: x = 0 = y, \end{aligned} \tag{2.9}$$

coincide with the x - and z -axis, respectively. They are visible and invisible, respectively, since

$$\begin{aligned} X^+(X^+f)(x, 0, 0) &= b + \mathcal{O}(x) > 0, \\ X^-(X^-f)(0, 0, z) &= |\beta| + \mathcal{O}(z) > 0. \end{aligned}$$

cf. (2.7). The two-fold singularity q is then placed at the origin:

$$q = (0, 0, 0).$$

Also, in (2.5) and (2.6), we have locally that

$$\begin{aligned} \Sigma_{sl} &: y = 0, xz > 0, \\ \Sigma_{cr} &: y = 0, xz < 0, \end{aligned} \tag{2.10}$$

where $\Sigma_{sl} = \Sigma_{sl}^- \cup \Sigma_{sl}^+$ with

$$\Sigma_{sl}^- : y = 0, x < 0, z < 0, \quad (\text{3rd quadrant of the } (x, z)\text{-plane})$$

and

$$\Sigma_{sl}^+ : y = 0, x > 0, z > 0, \quad (\text{1st quadrant of the } (x, z)\text{-plane})$$

being stable and unstable sliding regions, respectively. Similarly, $\Sigma_{cr} = \Sigma_{cr}^- \cup \Sigma_{cr}^+$ where

$$\Sigma_{cr}^- : y = 0, x > 0, z < 0, \quad (\text{2nd quadrant of the } (x, z)\text{-plane})$$

and

$$\Sigma_{cr}^+ : y = 0, x < 0, z > 0, \quad (\text{4th quadrant of the } (x, z)\text{-plane})$$

are regions with crossing downwards and upwards respectively (see Fig. 2.1).

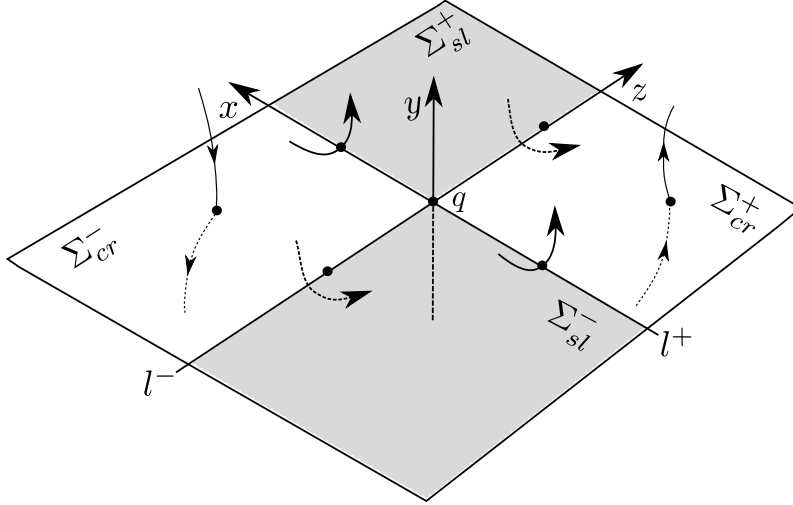


FIGURE 2.1. The thick dotted trajectories indicate tangencies of trajectories of X^- with the invisible fold line l^- . Similarly, the full trajectories illustrate the tangencies of X^+ with the visible fold line l^+ .

2.2. Canards of X_{sl} . The sliding vector-field X_{sl} of (2.5) and (2.6) within Σ_{sl} is by (2.2) given by

$$\begin{aligned} \dot{x} &= \sigma X_1^+(x, 0, z) + (1 - \sigma) X_1^-(x, 0, z), \\ \dot{y} &= 0, \\ \dot{z} &= \sigma X_3^+(x, 0, z) + (1 - \sigma) X_3^-(x, 0, z), \end{aligned} \quad (2.11)$$

with

$$\sigma = \frac{X^- f(x, 0, z)}{X^- f(x, 0, z) - X^+ f(x, 0, z)} = \frac{-|\beta|x + \mathcal{O}(z(x+z))}{-|\beta|x - bz + \mathcal{O}((x+z)^2)}. \quad (2.12)$$

The denominator of σ vanishes only at the two-fold within $\bar{\Sigma}_{sl}$. So we can re-parameterize time by multiplying the sliding vector field by $|X^- f(x, 0, z) - X^+ f(x, 0, z)|$ to obtain the following de-singularized sliding equations within Σ_{sl}^- :

$$\begin{aligned} \dot{x} &= -cx + bz + \mathcal{O}((x+z)^2) \\ \dot{z} &= -|\beta|x - \gamma z + \mathcal{O}((x+z)^2). \end{aligned} \quad (2.13)$$

Given (2.8) then the two-fold is a stable node of (2.13), with eigenvalues:

$$\lambda_{\pm} = -\frac{1}{2}(c + \gamma) \pm \frac{1}{2}\sqrt{(c - \gamma)^2 + 4b\beta}. \quad (2.14)$$

Notice that

$$\lambda_- < \lambda_+ < 0, \quad (2.15)$$

and the eigenvectors corresponding to λ_{\pm} are spanned by

$$v_{\pm} = \begin{pmatrix} 1 \\ -\chi_{\pm} \end{pmatrix}, \quad (2.16)$$

where

$$\chi_{\pm} = -\frac{1}{2b} \left(c - \gamma \pm \sqrt{(c - \gamma)^2 + 4b\beta} \right). \quad (2.17)$$

Here χ_{\pm} satisfies:

$$\chi_+ < \chi_- < 0, \quad (2.18)$$

cf. (2.8), and so the span of v_{\pm} is contained within $\Sigma_{sl} \cup \{0\}$. We therefore have the following proposition (see [15, Proposition 4.2]):

PROPOSITION 2.5. *Suppose (2.7) and (2.8). Then the following holds for the Filippov system (2.5) and (2.6):*

- (a) *There exists a unique strong canard γ^s tangent to v_- at the two fold;*
- (b) *There exists a funnel within Σ_{sl}^- , confined by the strong canard and the invisible fold line l^- , consisting of orbits that all pass through the two-fold tangent to v_+ .*

The sliding dynamics is shown in in Fig. 2.2. The funnel is shaded dark grey.

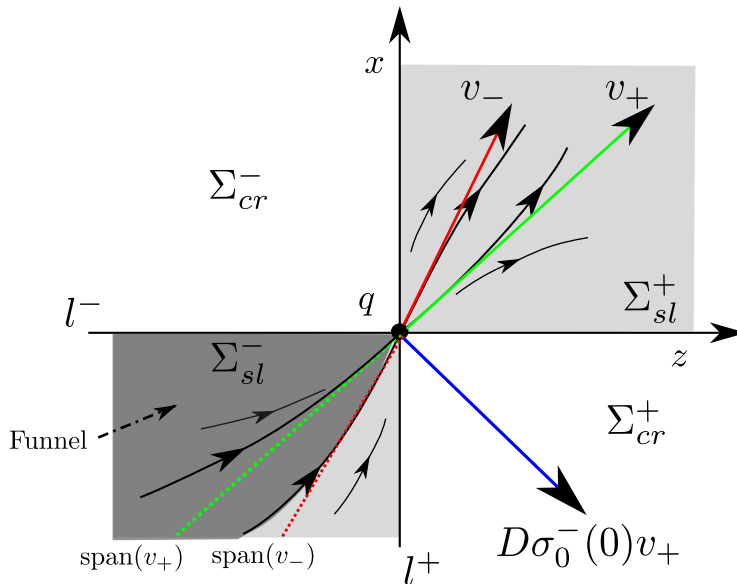


FIGURE 2.2. The sliding flow within Σ_{sl}^+ . The eigenvectors v_{\mp} are shown in red and green, respectively. The funnel (dark grey) is confined by the strong canard and the invisible fold line l^- . The mapping σ_0^- is defined in Proposition 2.6. The image $D\sigma_0^-(0)v_+$ (shown in blue) of v_+ under $D\sigma_0^-(0)$ is always contained outside the funnel.

2.3. A PWS mapping. In the sequel we will need the following proposition on the mapping

$$\sigma_0^- : \Sigma_{sl}^+ \rightarrow \Sigma$$

obtained as a first return to Σ using the forward flow of X^- . Note that this mapping is locally well-defined since l^- is invisible for X^- . See Fig. 2.1.

PROPOSITION 2.6. *The mapping σ_0^- satisfies the following:*

$$\sigma_0^-(x, z) = (-x + \mathcal{O}((x+z)^2), z + \frac{2\gamma}{b}x + \mathcal{O}((x+z)^2)), \quad (x, 0, z) \in \Sigma_{sl}^+.$$

In particular,

$$D\sigma_0^-(0)v_+ = \begin{pmatrix} -1 \\ z_1^* \end{pmatrix}, \quad (2.19)$$

with

$$z_1^* \equiv -\chi_+ + \frac{2\gamma}{b} > \chi_-. \quad (2.20)$$

Proof. This is a straightforward application of the implicit function theorem. The inequality for z_1^* in (2.20) is obtained from (2.17), the positivity of b and using (2.8). Indeed

$$b(z_1^* - \chi_-) = 2\gamma + c - \gamma = c + \gamma > \sqrt{(c - \gamma)^2 + 4b\beta} > 0$$

using (2.8) in the last two inequalities. \square

REMARK 2.7. *The consequence of (2.20) is that the vector $D\sigma_0^-(0)v_+$ in (2.19) is contained outside the funnel, after possibly restricting the small neighborhood \mathcal{U} further (see Fig. 2.2). Hence points close to span v_+ within Σ_{sl}^+ following X^- will either (a) enter Σ_{cr}^+ ($z_1^* > 0$) and cross upwards following X^+ , (b) enter Σ_{sl}^- and follow the sliding flow until l^+ where they leave through X^+ or exceptionally (c) enter l^+ from below and then leave by following the visible fold forward. This result will become very important later on.*

3. Regularization. As mentioned in section 1, our approach to establishing a deterministic notion for the visible-invisible two-fold is to use Sotomayor and Teixeira regularization (and so remove forward non-uniqueness), and use slow-fast theory and blowup to capture the limit as the regularization tends to zero. In this section, we recap the most relevant results of this approach as they relate to two-folds in \mathbb{R}^3 , following the work of the present authors [15]. We begin by defining the following class of regularization functions:

DEFINITION 3.1. *The C^k Sotomayor and Teixeira regularization functions*

$$\phi : \mathbb{R} \rightarrow \mathbb{R},$$

satisfy:

1° Finite deformation:

$$\phi(\hat{y}) = \begin{cases} 1 & \text{for } \hat{y} \geq 1, \\ \in (-1, 1) & \text{for } \hat{y} \in (-1, 1), \\ -1 & \text{for } \hat{y} \leq -1, \end{cases} \quad (3.1)$$

2° Monotonicity:

$$\phi'(\hat{y}) > 0 \quad \text{within } \hat{y} \in (-1, 1). \quad (3.2)$$

3° Finite C^k -smoothness: $\phi \in C^\infty$ within $\hat{y} \in (-1, 1)$ but there exists a smallest $k \geq 1$ so that $\phi^{(k+1)}$ is discontinuous at $\hat{y} = \pm 1$:

$$\begin{aligned} \lim_{\hat{y} \rightarrow 1^-} \phi^{(k+1)}(\hat{y}) &\neq 0, \\ \lim_{\hat{y} \rightarrow -1^+} \phi^{(k+1)}(\hat{y}) &\neq 0. \end{aligned}$$

REMARK 3.2. *Condition 3° is not in [22]. The reason for imposing the finite smoothness in 3° of Definition 3.1 is because the blowup method in the formulation of Krupa and Szmolyan [17] cannot be used to handle loss of hyperbolicity beyond algebraic order. We therefore need 3° in Appendix C.4. In [14] a study of the issues related to the C^∞ case is carried out and applied to a model of earthquake faulting in [3]. We are*

confident that the results of this paper can be extended to a more general class of monotonic regularization functions including, for example, \tanh .

An example of a C^1 Sotomayor and Teixeira regularization function is

$$\phi(\hat{y}) = -\frac{1}{2}\hat{y}^3 + \frac{3}{2}\hat{y} \quad \text{for } \hat{y} \in (-1, 1) \quad \text{and} \quad \phi(\hat{y}) = \pm 1 \quad \text{for } \hat{y} \gtrless \pm 1. \quad (3.3)$$

Here $\phi^{(1)}(\pm 1) = 0$ but $\lim_{\hat{y} \rightarrow 1^-} \phi^{(2)}(\hat{y}) = -3$ and $\lim_{\hat{y} \rightarrow -1^+} \phi^{(2)}(\hat{y}) = 3$ (while $\lim_{\hat{y} \rightarrow 1^+} \phi^{(2)}(\hat{y}) = \lim_{\hat{y} \rightarrow -1^-} \phi^{(2)}(\hat{y}) = 0$) and hence $k = 1$ in 3^o of Definition 3.1 for this example.

We then define the regularized vector-field $X_\epsilon(\mathbf{x})$ as

$$X_\epsilon(\mathbf{x}) = \frac{1}{2}X^+(\mathbf{x})(1 + \phi(\epsilon^{-1}y)) + \frac{1}{2}X^-(\mathbf{x})(1 - \phi(\epsilon^{-1}y)). \quad (3.4)$$

Note that

$$X_\epsilon(\mathbf{x}) = X^\pm(\mathbf{x}) \quad \text{for } y \gtrless \pm\epsilon, \quad (3.5)$$

due to 1^o of Definition 3.1. Using (2.5) and (2.6) the regularized system becomes:

$$\begin{aligned} \dot{x} &= (|\beta|^{-1}c + \mathcal{O}(x+y+z)) \left(1 + \phi\left(\frac{y}{\epsilon}\right)\right) + (-1 + \mathcal{O}(x+y+z)) \left(1 - \phi\left(\frac{y}{\epsilon}\right)\right), \\ \dot{y} &= (b + \mathcal{O}(x+y+z))z \left(1 + \phi\left(\frac{y}{\epsilon}\right)\right) + (-|\beta| + \mathcal{O}(x+y+z))x \left(1 - \phi\left(\frac{y}{\epsilon}\right)\right), \\ \dot{z} &= (1 + \mathcal{O}(x+y+z)) \left(1 + \phi\left(\frac{y}{\epsilon}\right)\right) + (b^{-1}\gamma + \mathcal{O}(x+y+z)) \left(1 - \phi\left(\frac{y}{\epsilon}\right)\right), \end{aligned} \quad (3.6)$$

after replacing time t by $2t$. Here $\epsilon \rightarrow 0$ is singular.

3.1. Initial blowup. We proceed as in [15, 16] by considering the following blowup:

$$y = \pi\bar{y}, \quad \epsilon = \pi\bar{\epsilon}, \quad (\pi, (\bar{y}, \bar{\epsilon})) \in \overline{\mathbb{R}^+} \times S^1. \quad (3.7)$$

and the chart $\bar{\epsilon} = 1$; see Fig. 3.2. This corresponds to setting $y = \hat{\pi}\hat{y}$, $\epsilon = \hat{\pi}$ or simply

$$\bar{\epsilon} = 1: \quad y = \epsilon\hat{y}, \quad \hat{y} \in \mathbb{R}, \quad \epsilon \geq 0. \quad (3.8)$$

Later (see e.g. section 5 and Appendix A) we will also use the following chart

$$\bar{y} = -1: \quad \epsilon = -y\hat{\epsilon}, \quad y \leq 0, \quad \hat{\epsilon} \geq 0, \quad (3.9)$$

also shown in Fig. 3.2. Notice that

$$\hat{\epsilon} = -\hat{y}^{-1},$$

for $\hat{y} < 0$, with \hat{y} defined by the chart $\bar{\epsilon} = 1$ in (3.8).

3.2. The chart $\bar{\epsilon} = 1$. Inserting (3.8) into (3.6) gives the following set of equations:

$$\begin{aligned} x' &= \epsilon \left((|\beta|^{-1}c + \mathcal{O}(x+\epsilon\hat{y}+z)) \left(1 + \phi(\hat{y})\right) + (-1 + \mathcal{O}(x+\epsilon\hat{y}+z)) \left(1 - \phi(\hat{y})\right) \right), \\ \hat{y}' &= (b + \mathcal{O}(x+\epsilon\hat{y}+z))z \left(1 + \phi(\hat{y})\right) + (-|\beta| + \mathcal{O}(x+\epsilon\hat{y}+z))x \left(1 - \phi(\hat{y})\right), \\ z' &= \epsilon \left((1 + \mathcal{O}(x+\epsilon\hat{y}+z)) \left(1 + \phi(\hat{y})\right) + (b^{-1}\gamma + \mathcal{O}(x+\epsilon\hat{y}+z)) \left(1 - \phi(\hat{y})\right) \right), \end{aligned} \quad (3.10)$$

with $(\cdot)' = \frac{d}{d\tau}$ and $\tau = \epsilon^{-1}t$. This is now a standard slow-fast system. The \hat{y} variable is fast with $\mathcal{O}(1)$ velocities whereas x and z are slow variables with $\mathcal{O}(\epsilon)$ velocities. The system (3.10) is called *the fast system*, whereas

$$\begin{aligned} \dot{x} &= \left((|\beta|^{-1}c + \mathcal{O}(x+\epsilon\hat{y}+z)) \left(1 + \phi(\hat{y})\right) + (-1 + \mathcal{O}(x+\epsilon\hat{y}+z)) \left(1 - \phi(\hat{y})\right) \right), \\ \epsilon\dot{\hat{y}} &= (b + \mathcal{O}(x+\epsilon\hat{y}+z))z \left(1 + \phi(\hat{y})\right) + (-|\beta| + \mathcal{O}(x+\epsilon\hat{y}+z))x \left(1 - \phi(\hat{y})\right), \\ \dot{z} &= \left((1 + \mathcal{O}(x+\epsilon\hat{y}+z)) \left(1 + \phi(\hat{y})\right) + (b^{-1}\gamma + \mathcal{O}(x+\epsilon\hat{y}+z)) \left(1 - \phi(\hat{y})\right) \right), \end{aligned} \quad (3.11)$$

is called *the slow system*. The limiting system $(3.10)_{\epsilon=0}$

$$\begin{aligned} x' &= 0, \\ \hat{y}' &= (b + \mathcal{O}(x + \epsilon \hat{y} + z))z(1 + \phi(\hat{y})) + (-|\beta| + \mathcal{O}(x + z))x(1 - \phi(\hat{y})), \\ z' &= 0, \end{aligned} \tag{3.12}$$

is called *the layer problem*, while $(3.11)_{\epsilon=0}$

$$\begin{aligned} \dot{x} &= (|\beta|^{-1}c + \mathcal{O}(x + z))(1 + \phi(\hat{y})) + (-1 + \mathcal{O}(x + z))(1 - \phi(\hat{y})), \\ 0 &= (b + \mathcal{O}(x + z))z(1 + \phi(\hat{y})) + (-|\beta| + \mathcal{O}(x + z))x(1 - \phi(\hat{y})), \\ \dot{z} &= ((1 + \mathcal{O}(x + z))(1 + \phi(\hat{y})) + (b^{-1}\gamma + \mathcal{O}(x + z))(1 - \phi(\hat{y}))), \end{aligned} \tag{3.13}$$

is called *the reduced problem*. The time τ is the *fast time* and time t is the *slow time*. Notice that x and z are constant in (3.12) whereas \hat{y} is slaved in (3.13).

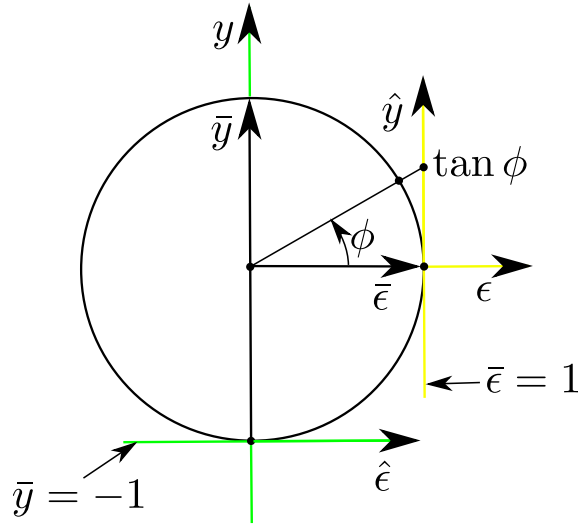


FIGURE 3.1. Illustration of the blowup (3.7) and the charts $\bar{\epsilon} = 1$ and $\bar{y} = -1$ using a projection onto the (ϵ, y) -plane.

3.3. Background. In this section we outline some results from [15] on the application of Fenichel's theory [8, 9, 10, 13] to (3.10). The starting point is the following result.

THEOREM 3.3. [15, Theorem 5.1, Proposition 5.4] *Let ϕ be a C^k Sotomayor and Teixeira regularization function. Then there exists a critical manifold*

$$S_0 = S_a \cup S_r \cup \hat{l}^+ \cup \hat{l}^- \cup \hat{q}$$

where

$$S_{a,r} : \hat{y} = h_{a,r}(x, z), \quad \text{for } (x, 0, z) \in \Sigma_{sl}^\pm, \tag{3.14}$$

with

$$h_a : \Sigma_{sl}^- \rightarrow \mathbb{R}, \quad h_r : \Sigma_{sl}^+ \rightarrow \mathbb{R},$$

defined by

$$\begin{aligned} h_{a,r}(x, z) &= \phi^{-1} \left(-\frac{X_2^+(x, 0, z) + X_2^-(x, 0, z)}{X_2^+(x, 0, z) - X_2^-(x, 0, z)} \right) \\ &= \phi^{-1} \left(-\frac{(|b| + \mathcal{O}(x + z))z + (-|\beta| + \mathcal{O}(x + z))x}{(|b| + \mathcal{O}(x + z))z - (-|\beta| + \mathcal{O}(x + z))x} \right), \end{aligned} \tag{3.15}$$

respectively, and

$$\hat{l}^- = \{(x, \hat{y}, z) | x = 0, \hat{y} = -1, z \neq 0\}, \quad \hat{l}^+ = \{(x, \hat{y}, z) | x \neq 0, \hat{y} = 1, z = 0\}, \quad (3.16)$$

$$\hat{q} = \{(x, \hat{y}, z) | \hat{y} \in \mathbb{R}, x = 0, z = 0\}, \quad (3.17)$$

of (3.10) $_{\epsilon=0}$. On $S_{a,r}$ the motion of the slow variables x and z is described by (3.13) which coincides with the sliding equations (2.11). Also S_a is normally attracting, S_r is normally repelling while \hat{l}^\pm and \hat{q} are non-normally hyperbolic critical points of (3.10).

Proof. The critical manifold is a set of equilibria of (3.12). The hyperbolicity is determined by the linearization of (3.12). The non-normally hyperbolicity of \hat{l}^\pm is a consequence of 3 $^\circ$ in Definition 3.1. \square

The critical manifold is illustrated in Fig. 3.2. The PWS fold lines l^\pm give rise to the lines \hat{l}^\pm , in (3.16), of nonhyperbolic critical points of the regularized system. Similarly, the PWS two-fold point q becomes the line \hat{q} , in (3.17), of nonhyperbolic critical points. If we *scale back down* and return to our original y variable using (3.8) then the critical manifolds $S_{a,r}$ become graphs $y = \epsilon h_{a,r}(x, z)$ within $(x, z) \neq 0$. For $\epsilon = 0$ the whole of S_0 therefore collapses to $\bar{\Sigma}_{sl}$ within $y = 0$ and we recover the PWS Filippov system. In particular, \hat{l}^\pm and \hat{q} collapse to l^\pm and q , respectively.

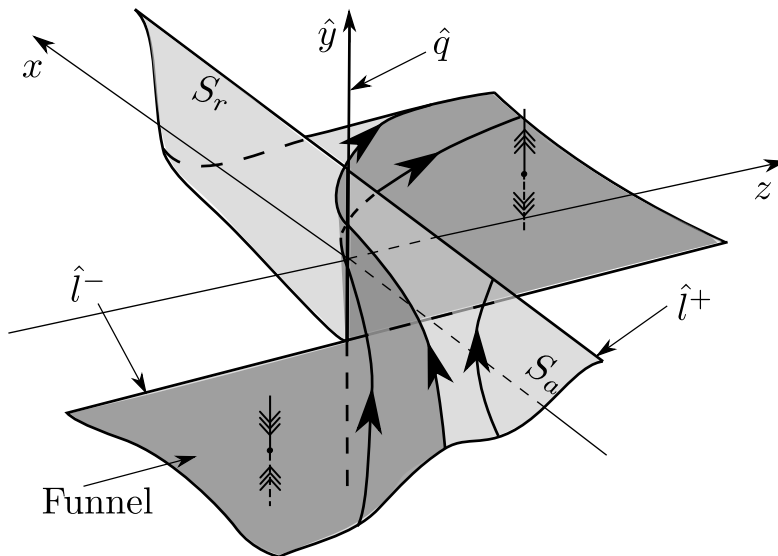


FIGURE 3.2. The critical manifold described in Theorem 3.3.

Fenichel's theory applies away from both the fold lines \hat{l}^\pm of (3.16) and the line \hat{q} of (3.17). In the following proposition, we collect the results of the application of Fenichel's theory:

PROPOSITION 3.4. *Let $\mathcal{U}^- \subset \{(x, z)\}$ and $\mathcal{U}^+ \subset \{(x, z)\}$ be compact regions completely contained within the third ($x < 0, z < 0$) and first quadrants ($x > 0, z > 0$), respectively. Then the critical manifolds*

$$S_a|_{\mathcal{U}^-} : \hat{y} = h_a(x, z), (x, z) \in \mathcal{U}^-,$$

$$S_r|_{\mathcal{U}^+} : \hat{y} = h_r(x, z), (x, z) \in \mathcal{U}^+,$$

perturb to locally invariant slow manifolds

$$S_{a,\epsilon} : y = h_{a,\epsilon}(x, z, \epsilon) = h_a(x, z) + \mathcal{O}(\epsilon), (x, z) \in \mathcal{U}^-,$$

$$S_{r,\epsilon} : y = h_{r,\epsilon}(x, z, \epsilon) = h_r(x, z) + \mathcal{O}(\epsilon), (x, z) \in \mathcal{U}^+$$

for $\epsilon \ll 1$ sufficiently small. In general, $S_{a,\epsilon}$ and $S_{r,\epsilon}$ are non-unique but they are all $\mathcal{O}(e^{-c/\epsilon})$ -close for some $c > 0$ independent of ϵ . The flow on $S_{a,\epsilon}$ and $S_{r,\epsilon}$ is ϵ -close to the flow of the sliding equations (2.11).

Using the blowup method, it is shown in [15] that the Fenichel slow manifolds $S_{a,\epsilon}$ and $S_{r,\epsilon}$ can be extended as perturbations of S_a and S_r , respectively, up to an $\sqrt{\epsilon}$ -neighborhood of the two-fold. We will denote the extensions by the same symbols. Then we let $S_{a,\epsilon}^t$ ($S_{r,\epsilon}^{-t}$) denote the extension of $S_{a,\epsilon}$ ($S_{r,\epsilon}$) by the forward (backward) flow. The main result (Theorem 7.1) in [15] is then the following:

THEOREM 3.5. *Let ϵ be sufficiently small, fix copies of $S_{a,\epsilon}$ and $S_{r,\epsilon}$, and suppose that the following non-resonance condition holds*

$$\xi \equiv \lambda_+^{-1} \lambda_- \notin \mathbb{N}. \quad (3.18)$$

Then there exists a weak canard $\gamma^w(\epsilon)$ and a strong canard $\gamma^s(\epsilon)$, satisfying $\gamma^{w,s}(\epsilon) \subset S_{a,\epsilon}^t \cap S_{r,\epsilon}^{-t}$, with the following properties:

- $\gamma^s(0)$ is tangent to the eigenvector v_- at the two-fold singularity.
- $\gamma^w(0)$ is tangent to the eigenvector v_+ at the two-fold singularity.

3.4. The weak canard. As opposed to the strong canard γ^s , the limit $\gamma^w(0)$ of the weak canard $\gamma^w(\epsilon)$, cannot be identified within the critical manifolds $S_{a,r}$ and the PWS Filippov system. There is a whole funnel of singular weak canard candidates. Hence a priori, for general initial conditions within the funnel, it is impossible to determine on what side of the canard the initial conditions are. This is (in principle) important for our purposes because by the transversal intersection of $S_{a,\epsilon}$ and $S_{r,\epsilon}$ along the weak canard, initial conditions on either side of the weak canard will jump in opposite directions from the repelling slow manifold $S_{r,\epsilon}$ and therefore eventually follow X^+ or X^- . Similar issues arise with weak canards of folded nodes in standard slow-fast systems in \mathbb{R}^3 , see [4, 24]. However, we will show that *macroscopically*, that is on the scale of (x, y, z) , initial conditions on either side of the weak canard $\gamma^w(\epsilon)$ behave similarly. If initial conditions jump in the direction of Σ^- and follow X^- then they will return to Σ^+ and follow X^+ after a small twist. This is a consequence of the crucial Proposition 2.6 (see also Remark 2.7).

4. Main result. Since there is a lot of technical detail in what follows, we will now give the reader a clear idea of where we are headed. So far, we have a visible-invisible two-fold in our PWS Filippov system described locally by (2.5) and (2.6) satisfying (2.7) and (2.8) and the regularized version of this system (3.10). Now we assume that the PWS system has a closed cycle Γ , which we call a *closed PWS singular cycle*; see both assumption (A) and Fig. 4.1 below. Then the main result of the paper, Theorem 4.1, is that the regularized system, under further mild assumptions (B) and (C) which we state below, has a limit cycle Γ^ϵ satisfying $\lim_{\epsilon \rightarrow 0} \Gamma^\epsilon = \Gamma$ and that Γ^ϵ attracts almost every orbit passing near the two-fold through the funnel region.

We assume the following about the PWS system (2.5) and (2.6):

- (A) There exists a *closed PWS singular cycle* $\Gamma = U \cup D \cup F$, see Fig. 4.1, of the PWS Filippov system (X^+, X^-) , described locally near q by (2.5) and (2.6) satisfying (2.7) and (2.8), consisting of the following:

- A solution curve

$$U(t) = (x(t), y(t), z(t))_{t \in [0, T_1]} \subset \bar{\Sigma}^+, \quad (4.1)$$

of the system $X^+|_{y \geq 0}$ satisfying $U(0) = 0$ and

$$u \equiv U(T_1) \in \Sigma_{cr}^-. \quad (4.2)$$

- A solution curve

$$D(t) = (x(t), y(t), z(t))_{t \in [T_1, T_2]} \subset \bar{\Sigma}^-, \quad (4.3)$$

of the system $X^-|_{y \leq 0}$ satisfying $D(T_1) = u$ and

$$d \equiv D(T_2) \in \Sigma_{sl}^-, \quad (4.4)$$

with d contained inside the funnel.

– A solution curve

$$F(t) = (x(t), 0, z(t))_{t \in [T_2, T_3]} \subset \Sigma_{sl}^- \cup q, \quad (4.5)$$

of the sliding equations, contained within the *funnel* (shaded area in Fig. 4.1), and satisfying

$$F(T_2) = d, \quad F(T_3^-) = q. \quad (4.6)$$

(B) The non-degeneracy condition (3.18)

$$\xi \equiv \lambda_+^{-1} \lambda_- \notin \mathbb{N}, \quad (4.7)$$

used in Theorem 3.5, holds.

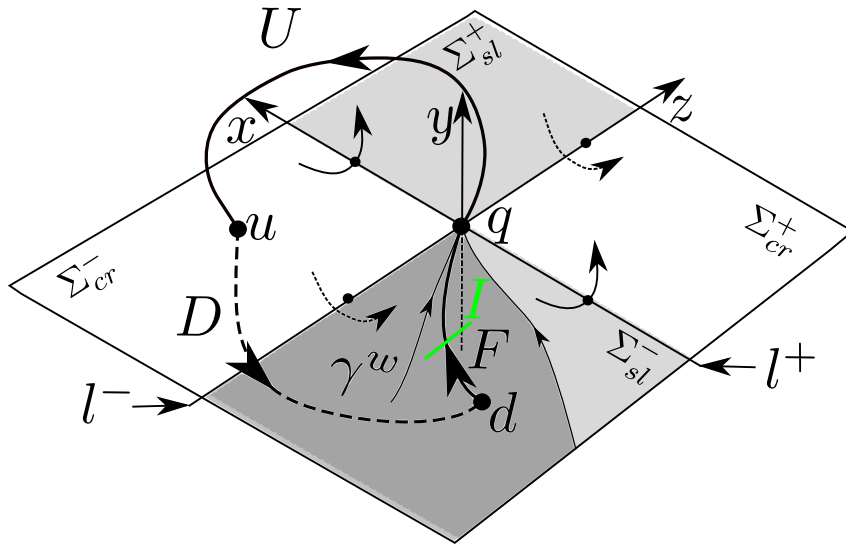


FIGURE 4.1. The singular cycle $\Gamma = U \cup D \cup F$. The interval I will be important in the proof of Theorem 4.1. See e.g. Appendix A.

We assume the following about the regularized system (3.10):

(C) There exists a $K > 0$ sufficiently large so that

$$\text{dist}(d, \gamma^w(\epsilon)) \geq K^{-1} > 0,$$

for all $\epsilon \leq \epsilon_0$ sufficiently small.

The main result of the paper is then:

THEOREM 4.1. *Let ϕ be a C^k Sotomayor and Teixeira regularization function. Suppose (A), (B), and (C) all hold and also let V be any compact set contained within the funnel which satisfies $\gamma^w(0) \notin V$. Then there exists an $\epsilon_0 > 0$ so that for $\epsilon \leq \epsilon_0$ there exists an attracting limit cycle Γ^ϵ of X_ϵ satisfying:*

$$\Gamma^\epsilon \rightarrow \Gamma,$$

in the Hausdorff distance and in addition Γ^ϵ attracts all initial conditions from V .

REMARK 4.2. *Condition (A) requires a return mechanism from the two-fold, by crossing only, to the funnel. This is clearly generic. The requirement that d is contained within the funnel guarantees transversality to Σ_{sl}^- . Note that d can not lie on l^- , since the latter is a line of folds. Condition (B) and (C) are non-degeneracy conditions. It would have been nice to replace the condition (C) with a condition for $\epsilon = 0$. But we did not find a way to do this.*

REMARK 4.3. *There may exist other intersections of $S_{a,\epsilon}$ and $S_{r,\epsilon}$ (secondary canards) as the numerics in [15] indicate. However, we do not need to include an assumption on d relative to these orbits. Indeed,*

it follows from the blowup analysis in [15], using an identical argument to that used in [4], that all other (potential) intersections of $S_{a,\epsilon}$ and $S_{r,\epsilon}$ (secondary canards) converge to the strong canard as $\epsilon \rightarrow 0$.

Theorem 4.1 provides a consistent interpretation of the visible-invisible two-fold. See also Proposition 5.5 below. Note that there are two separate cases to consider. The sliding segment F may lie between the invisible fold line l^- and the weak canard $\gamma^w(0)$ or between $\gamma^w(0)$ and the strong canard $\gamma^s(0)$. In Fig. 4.1 we have shown the segment F lying between $\gamma^w(0)$ and $\gamma^s(0)$. We will see that the difference between the two cases in the next section. Note that, with the exception of the weak canard $\gamma^w(0)$, Γ^0 attracts the whole funnel.

We prove Theorem 4.1 in section 6. We lay out our approach and give important lemmata and propositions in the following section.

5. Existence of a limit cycle. In order to prove Theorem 4.1, we proceed as follows. First in section 5.1 we translate (parts of) the singular cycle Γ of the PWS system into (parts of) a singular cycle Γ^0 of the regularization. We will show that this leads to a gap in Γ^0 . To close this gap and complete a closed singular cycle of the regularized system, we apply blowup and desingularization. We outline our approach and the results of our analysis in section 5.2. Finally we define a return mapping \mathcal{P}_ϵ in section 5.3. We will compose this return mapping into two parts: A global mapping \mathcal{G}_ϵ , which will be described by Fenichel's theory directly, and a local mapping \mathcal{L}_ϵ which we describe using the blowup in section 5.2.

5.1. The cycle Γ^0 . To describe the singular cycle Γ^0 of the regularization we first use the blowup (3.7), the chart $y = \epsilon \hat{y}$ in (3.8) and the limiting systems in (3.12) and (3.13) for $\epsilon = 0$. However, the flows of X^\pm are clearly not observable within either of these limiting systems. Instead it is hidden at $\hat{y} = \pm\infty$, corresponding to the north and the south pole $\bar{y} = \pm 1$ of the blowup circle $(\bar{y}, \bar{\epsilon}) \in S^1$ in (3.7). To cover $\bar{y} = \pm 1$ of the blowup (3.7) and connect the orbits of (3.12) and (3.13) with the orbits of X^\pm , one could use the corresponding charts, such as $\bar{y} = -1$ in (3.9). But due to the *finite deformation* of the regularization functions in Definition 3.1, in particular the special structure in (3.5), it is often easier to just *scale back down* and return to y and the systems X^\pm (as it was done in [16]) whenever $\hat{y} \notin (-1, 1)$, corresponding to $y \notin (-\epsilon, \epsilon)$ for $\epsilon > 0$ using (3.8). Geometrically, we therefore blowup the plane $y = 0$ to $\hat{y} \in [-1, 1]$ for $\epsilon = 0$.¹ Within $\hat{y} \in (-1, 1)$ we follow slow-fast theory and concatenate orbits of the layer problem (3.12) with orbits of the reduced problem (3.13), respecting the direction of time. Following this approach we obtain the following (see Fig. 5.1):

- Segment U , from assumption (A), departing from the two fold and terminating at

$$u \equiv (u_x, 0, u_z) \in \Sigma_{cr}^-.$$

- Segment \widehat{UD} consisting of a *vertical* orbit segment of the layer equations (3.12) connecting $\hat{y} = 1$ with $\hat{y} = -1$:

$$\widehat{UD} = \{(u_x, \hat{y}, u_z) | \hat{y} \in [-1, 1]\}.$$

- Segment D , from assumption (A), departing from u and terminating at

$$d \equiv (d_x, 0, d_z) \in \Sigma_{sl}^-.$$

- Segment \widehat{DF} consisting of a *vertical* orbit segment of the layer equations (3.12) connecting

$$d = (d_x, -1, d_z) \in \{\hat{y} = -1\},$$

with

$$(d_x, \hat{y}^*, d_z) \in S_a, \tag{5.1}$$

in forward time², where

$$\hat{y}^* = h_a(d_x, d_z) \in (-1, 1).$$

¹If the set of regularization functions is extended to include functions such as the analytic one

$$\phi(x) = \tanh(x),$$

with $\phi(x) \neq \pm 1$, then the *finite deformation* condition in Definition 3.1 is violated. To proceed, the charts $\bar{y} = \pm 1$ would need to be included (see [14] for details).

²Note that (5.1) is an attracting equilibrium of the layer problem (3.12), with x and z as parameters, cf. also (3.14).

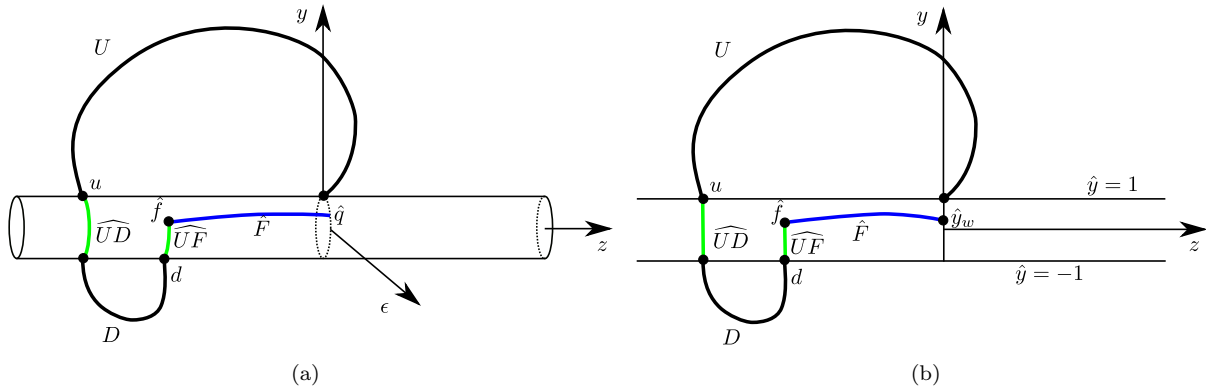


FIGURE 5.1. (a): Projection onto the (z, y) -plane of segments of the closed singular cycle Γ^0 that can be identified using the blowup (3.7), the layer problem (3.12) and the reduced problem (3.13). We insert the cylinder that occurs due to the blowup (3.7). In (b) we take the other point of view, described in section 5.1, using the chart $y = \epsilon \hat{y}$ and the property (3.5) to blowup $y = 0$ to the strip $\hat{y} \in [-1, 1]$ for $\epsilon = 0$. For simplicity we use the same notation in (a) and in (b). There is a gap between the end of \hat{F} and the start of U , see Lemma 5.1. We close this gap using the blowup in (5.3). The notation is explained in the text. The two-fold itself has now become the nonhyperbolic line \hat{q} , defined in (3.17).

- Segment \hat{F} of the reduced problem (3.13), which (cf. Proposition 3.4) is just $F \subset \{y = 0\}$ of assumption (A) projected onto the critical manifold S_a .

The connections described by \widehat{UD} and \widehat{DF} occur instantaneously on the slow time scale t .

The components of Γ^0 identified above do not give a closed cycle in the blowup space (3.7):

LEMMA 5.1. *The closure of $\hat{F} \subset \{x < 0, z < 0\}$ intersects \hat{q} in*

$$\overline{\hat{F}} \cap \hat{q} = \{x = z = 0, \hat{y} = \hat{y}_w\},$$

where

$$\hat{y}_w \equiv \phi^{-1} \left(\frac{1 + |\beta|^{-1} b \chi_+}{1 - |\beta|^{-1} b \chi_+} \right) \in (-1, 1). \quad (5.2)$$

Proof. The projection of \hat{F} onto the (x, z) plane is tangent to the vector v_+ (2.16) by assumption (A). The \hat{y} -variable is described by $h_a(x, z)$ in (3.15). Letting $z = -\chi_+ x \rightarrow 0^-$ gives

$$\hat{y} = \phi^{-1} \left(\frac{1 + |\beta|^{-1} b \chi_+}{1 - |\beta|^{-1} b \chi_+} \right).$$

Finally $\hat{y} \in (-1, 1)$ by 2° in Definition 3.1 and $\chi_+ < 0$; see (2.18). \square

Hence there is a gap between the end of $\hat{F} \subset \{-1 < \hat{y} < 1\}$ and the start of U within $\hat{y} = 1$. To close this gap and complete the singular cycle Γ^0 we blowup the nonhyperbolic line \hat{q} .

5.2. Closing the gap. Following [15] we blowup the line \hat{q} by

$$x = r\bar{x}, z = r\bar{z}, \epsilon = r^2\bar{\epsilon}, \quad (r, (\bar{x}, \bar{z}, \bar{\epsilon})) \in \mathbb{R}_+ \times S^2, \quad (5.3)$$

within the chart (3.8). Note that \hat{y} is not transformed by this blowup and hence geometrically (5.3) replaces the line \hat{q} with a cylinder of spheres

$$r = 0, \hat{y} \in \mathbb{R}, (\bar{x}, \bar{z}, \bar{\epsilon}) \in S^2. \quad (5.4)$$

The sphere:

$$S_w^2 : r = 0, \hat{y} = \hat{y}_w, (\bar{x}, \bar{z}, \bar{\epsilon}) \in S^2, \quad (5.5)$$

within $\hat{y} = \hat{y}_w$ (5.2), will be important in the following.

We consider the following charts:

$$\kappa_1 : \bar{x} = -1 : \quad x = -r_1, z = r_1 z_1, \epsilon = r_1^2 \epsilon_1, \quad (5.6)$$

$$\kappa_2 : \bar{\epsilon} = 1 : \quad x = r_2 x_2, z = r_2 z_2, \epsilon = r_2^2, \quad (5.7)$$

$$\kappa_3 : \bar{x} = 1 : \quad x = r_3, z = r_3 z_3, \epsilon = r_3^2 \epsilon_3, \quad (5.8)$$

the associated coordinate changes:

$$\kappa_{21} : \kappa_1 \rightarrow \kappa_2 : \quad x_2 = -1/\sqrt{\epsilon_1}, r_2 = r_1 \sqrt{\epsilon_1}, z_2 = z_1/\sqrt{\epsilon_1}, \quad (5.9)$$

$$\kappa_{32} : \kappa_2 \rightarrow \kappa_3 : \quad r_3 = r_2 x_2, z_3 = x_2^{-1} z_2, \epsilon_3 = x_2^{-2}, \quad (5.10)$$

defined for $\epsilon_1 > 0$, $x_2 > 0$, respectively, and their inverses $\kappa_{12} = \kappa_{21}^{-1}$ and $\kappa_{23} = \kappa_{32}^{-1}$. The charts are visualized in Fig. 5.2. We abuse notation by using the same symbol κ_i , $i = 1, 2, 3$, to refer to both the chart itself and the mappings $(x, z, \epsilon) \mapsto (r_1, z_1, \epsilon_1)$, (x_2, z_2, r_2) and (r_3, z_3, ϵ_3) . We follow the (standard) convention that variables, manifolds, and other dynamical objects will be given a subscript i in chart κ_i . For example, we denote \hat{F} by \hat{F}_1 in chart κ_1 . An object, say M_i obtained in chart κ_i , will be denoted by \bar{M} in the blowup variables (5.3).

The transformation (5.3) pulls back the regularized vector-field X_ϵ (3.10) to a vector-field \bar{X} on

$$(\hat{y}, r, (\bar{x}, \bar{z}, \bar{\epsilon})) \in \mathbb{R} \times \overline{\mathbb{R}}_+ \times S^2.$$

Here $\bar{X}|_{r=0} = 0$. We study this system divided by r :

$$\tilde{X} \equiv r^{-1} \bar{X}, \quad (5.11)$$

which desingularizes the dynamics within the blowup of \hat{q} (5.4); see [15]. This enables us to connect \hat{F} with U by following separate orbit segments that we will introduce shortly. These new segments will be denoted by \bar{Q}^α in the blowup variables (5.3) and by $Q_{1,2,3}^\alpha$ in charts $\kappa_{1,2,3}$ respectively³. As we discussed in section 4, there are two separate cases to consider, depending on the position of the sliding segment F , relative to the fold line l^- and the canards $\gamma^{s,w}(0)$, and, as we shall see below, the ratio of the eigenvalues ξ (3.18).

DEFINITION 5.2. *Let $n = \lfloor \xi \rfloor$ be the greatest integer less than ξ , the ratio of the eigenvalues, see (4.7). Then we define the following two cases:*

- *Case (i):*
 - F is between $\gamma^w(0)$ and $\gamma^s(0)$ and n is even,
 - or
 - F is between l^- and $\gamma^w(0)$ and n is odd.
- *Case (ii):*
 - F is between $\gamma^w(0)$ and $\gamma^s(0)$ and n is odd,
 - or
 - F is between l^- and $\gamma^w(0)$ and n is even.

We now summarize the results of the analysis in the following sections and appendices. The two cases (i) and (ii) give rise to separate singular cycles Γ^0 which we illustrate in Fig. 5.2 and Fig. 5.3, respectively. These figures are representations of the dynamics, which occurs in \mathbb{R}^4 . We have inserted the blowup of the line of non-hyperbolic fixed points \hat{q} as the cylinder of spheres (5.4) within $\hat{y} \in [-1, 1]$, highlighting the sphere S_w^2 (5.5) at $\hat{y} = \hat{y}_w$. The lids of the cylinder at $\hat{y} = \pm 1$ both collapse to the point $(x, y, z) = 0$ when we blow and scale back down.

The manifolds S_a and S_r intersect transversally along $\gamma^w(0)$ upon blowup, see Theorem 3.5. Variations within the tangent spaces $T_{\gamma^w(0)} S_a \setminus \{\dot{\gamma}^w(0)\}$ will therefore align themselves with the unstable fibers of S_r and jump in opposite directions under the forward variational flow. The number ξ describes the number of rotations of the tangent space (see Lemma A.1). Case (i) in Fig. 5.2 then corresponds to the case where the forward flow of \hat{F} is *above* S_r as $\epsilon \rightarrow 0$. The repulsion of S_r therefore takes \hat{F} upwards following first

³Note that the superscript α is a simple counter. It has nothing to do with any chart.

\overline{Q}^1 across the blowup sphere S_w^2 and then $\overline{Q}^{2,+}$ back to the lid $\hat{y} = 1$ and the start of U . For case (ii) in Fig. 5.3, on the other hand, the forward flow of \hat{F} is *below* S_r as $\epsilon \rightarrow 0$ following $\overline{Q}^{2,-}$ downwards. This is then followed by a *twist* before returning to the top lid $\hat{y} = 1$.

\overline{Q}^3 in Fig. 5.3 is only visible in the chart $\bar{y} = -1$ of $\bar{\epsilon} = 1$ in (3.7). See Fig. A.3 below. In the blown down variables (x, y, z) , for example, it just collapses to $(x, y, z) = 0$ whereas in chart $\bar{\epsilon} = 1$ of (3.7) it sits at $\hat{y} = -\infty$.

The details of the twist in case (ii) further depend on what side of \hat{l}^+ the end of \overline{Q}^3 belongs to. This is determined by the value of z_1^* (2.20) in Proposition 2.6, see also Remark 2.7. In Fig. 5.3, when $z_1^* < 0$, we illustrate the more complicated case where \overline{Q}^3 re-injects the singular cycle into the blowup region corresponding to stable sliding. The geometry of the visible-invisible two-fold restricts this re-injection to occur outside the funnel between the strong canard $\gamma^s(0)$ and the visible fold l^+ (since $z_1^* > \chi_+$ cf. Proposition 2.6). The blowup of the reduced dynamics on \overline{L}_a : the extension of S_a onto the blowup cylinder, therefore pushes (see \overline{Q}^5) this re-injection towards \hat{l}^+ . Recall Fig. 2.2: points between $\gamma^s(0)$ and l^+ eventually leave the sliding region through the visible fold l^+ . When $z_1^* > 0$, the segment \overline{Q}^3 re-injects the singular cycle into the region corresponding to crossing upwards (see Fig. 2.2). This case is not illustrated. In Fig. 5.3, it corresponds to removing \overline{Q}^5 and letting \overline{Q}^4 (whose projection onto the (\bar{x}, \bar{z}) -plane is now contained within Σ_{cr}^+) connect $\{\hat{y} = -1\}$ with $\{\hat{y} = 1\}$ directly. The exceptional case $z_1^* = 0$ looks similar except now $\overline{Q}^4 \subset \{\bar{z} = 0\}$.

5.3. Return mapping. Consider the section $\{x = -\rho\}$. The reduced flow within Σ_{sl}^- is transverse to this section for ρ sufficiently small. Let $I \subset \mathbb{R}$ be a compact interval so that the graph of $h_a|_{\{-\rho\} \times I}$ is:

- A closed neighborhood of $\hat{F} \cap \{x = -\rho\}$ contained within the funnel;
- Bounded away from the weak canard $\gamma^w(0)$.

See Fig. 4.1 and Fig. 5.2. Then we define the following sections:

$$\begin{aligned} \Upsilon &= \{(x, y, z) \mid y = \epsilon, |x|, |z| \leq v\} \subset \{y = \epsilon\}, \\ \Delta &= \{(x, y, z) \in \mathcal{U} \mid x = -\rho, z \in I, y \in [-\epsilon, \epsilon]\} \subset \{x = -\rho\}, \end{aligned}$$

with v and ρ small. In (x, \hat{y}, z) -space they take the following form:

$$\begin{aligned} \hat{\Upsilon} &= \{(x, \hat{y}, z) \mid \hat{y} = 1, |x|, |z| \leq v\}, \\ \hat{\Delta} &= \{(x, \hat{y}, z) \in \mathcal{U} \mid x = -\rho, z \in I, \hat{y} \in [-1, 1]\}. \end{aligned}$$

See Fig. 5.2. Points within Υ are parametrized by (x, z) since $y = \epsilon$ (or $\hat{y} = 1$) is fixed. We shall therefore for simplicity write $(x, z) \in \Upsilon$ (rather than $(x, \epsilon, z) \in \Upsilon$). We adopt a similar notation on e.g. $\hat{\Upsilon}$, Δ , and $\hat{\Delta}$ henceforth. We then define the following return mapping

$$\mathcal{P}_\epsilon : \Upsilon \ni (x, z) \mapsto (x_+, z_+) = \mathcal{P}_\epsilon(x, z) \in \Upsilon,$$

defined by the forward flow of X_ϵ . We will show that this mapping is well-defined for v sufficiently small and that it is a contraction on Υ . To do this we split \mathcal{P}_ϵ up into two parts; a global part \mathcal{G}_ϵ and a local part \mathcal{L}_ϵ where

$$\mathcal{G}_\epsilon : \Upsilon \ni (x, z) \mapsto (y_+, z_+) = \mathcal{G}_\epsilon(x, z) \in \Delta, \quad (5.12)$$

$$\mathcal{L}_\epsilon : \Delta \ni (y, z) \mapsto (x_+, z_+) = \mathcal{L}_\epsilon(y, z) \in \Upsilon. \quad (5.13)$$

Then

$$\mathcal{P}_\epsilon = \mathcal{L}_\epsilon \circ \mathcal{G}_\epsilon.$$

LEMMA 5.3. *Suppose (A). Then for v sufficiently small, then the PWS system has a well-defined mapping*

$$G_0 : \Upsilon \ni (x, z) \mapsto (y_+, z_+) = G_0(x, z) \in \Delta,$$

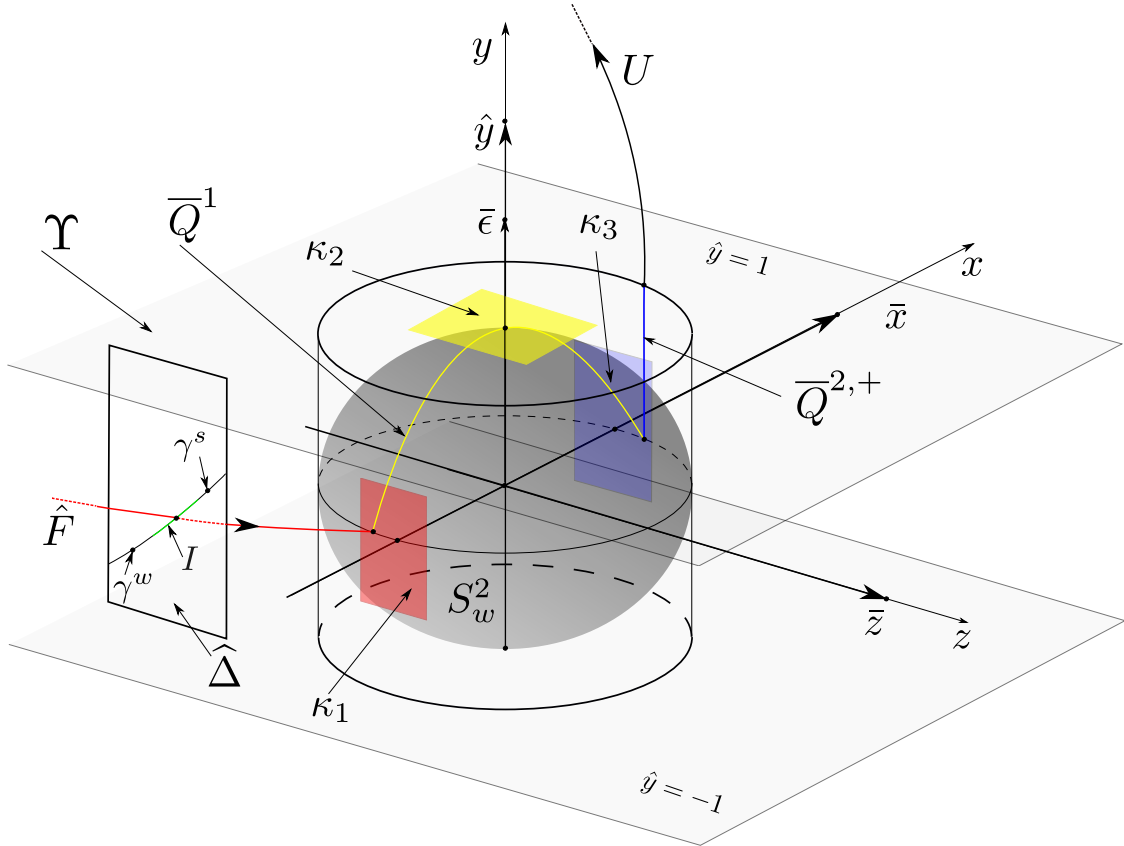


FIGURE 5.2. Close-up of part of the closed singular cycle Γ^0 for case (i). The segment \overline{Q}^1 lies on the sphere S_w^2 (5.5) of the blowup of \hat{q} defined through (5.3). The segment $\overline{Q}^{2,+}$ is vertical (purely in the \hat{y} -direction). Chart $\kappa_1 : \bar{x} = -1$ is shown in red, chart $\kappa_2 : \bar{y} = 1$ in yellow and chart $\kappa_3 : \bar{x} = 1$ in blue. The connection from U to \hat{F} is shown in Fig. 5.1.

as a composition of the forward flow of X_+ , X^- (2.1) and finally X_{sl} (2.2). In particular, $G_0(\Upsilon)$ is one-dimensional and G_0 maps $q = U \cap \Upsilon = U \cap \{y = 0\}$ to $F \cap \Delta = F \cap \{x = -\rho\}$.

Proof. Follows directly from (A) and smooth dependency of initial conditions. \square

We can then describe \mathcal{G}_ϵ as follows.

PROPOSITION 5.4. *Suppose (A) and (C). For v sufficiently small, then there exists an $\epsilon_0 > 0$ so that for every $\epsilon \leq \epsilon_0$ the following holds true:*

- (a) $\mathcal{G}_\epsilon(x, z)$ is $\mathcal{O}(\epsilon)$ -close to the associated mapping $G_0(x, z)$ of the PWS system.
- (b) The Jacobian $D\mathcal{G}_\epsilon$ satisfies $\|D\mathcal{G}_\epsilon\| = \mathcal{O}(1)$.
- (c) $\text{dist}(\mathcal{G}_\epsilon(\Upsilon) - h_{a,\epsilon}|_{\{-\rho\} \times \mathbb{R}_-}) = \mathcal{O}(e^{-c/\epsilon})$.
- (d) The image $\mathcal{G}_\epsilon(\Upsilon)$ is uniformly bounded away from $\gamma^w(\epsilon) \cap \Delta$ as $\epsilon \rightarrow 0$.

Proof. Properties (a), (b) and (c) follow directly from Lemma 5.3 and Fenichel's theory. Recall Proposition 3.4. Property (d) follows from assumption (C). \square

We describe \mathcal{L}_ϵ in the following proposition:

PROPOSITION 5.5. *Suppose (B) and (C). Then for $\epsilon \ll 1$ the mapping \mathcal{L}_ϵ is well-defined and satisfies:*

$$\mathcal{L}_\epsilon(y, z) = o(1), \quad D\mathcal{L}_\epsilon(y, z) = o(1), \quad (5.14)$$

for all $(y, z) \in \Delta$.

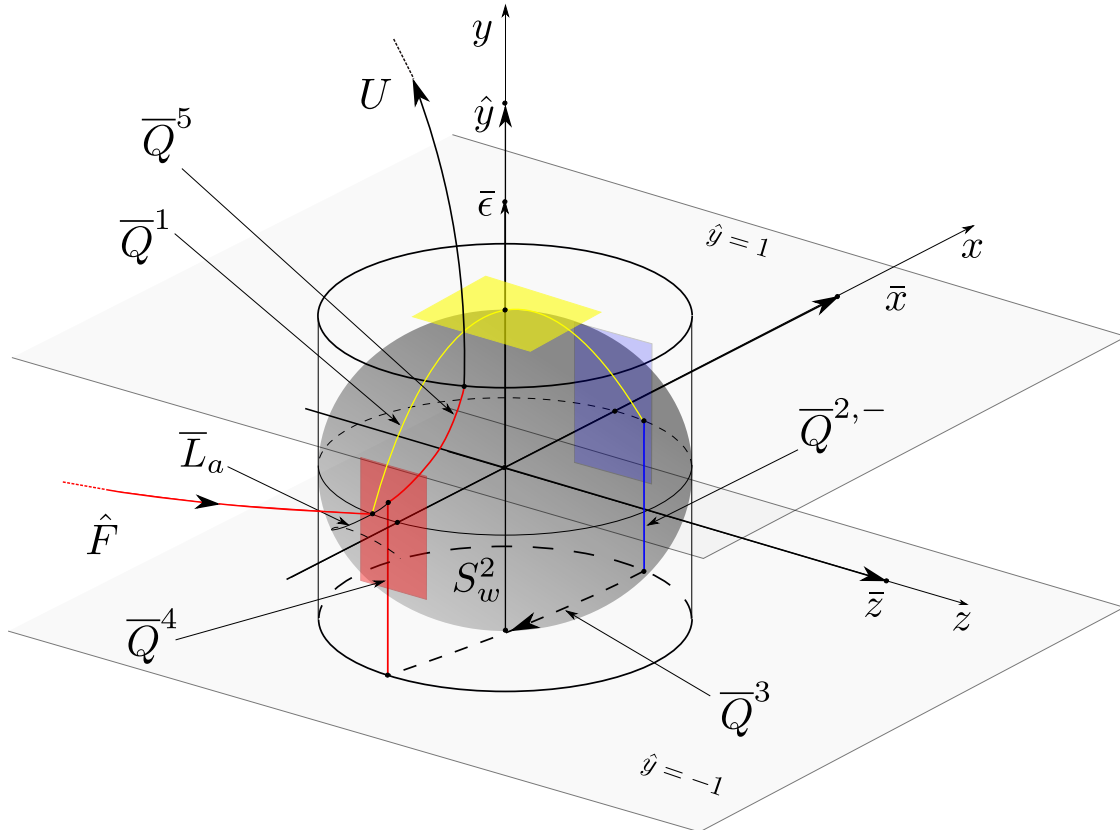


FIGURE 5.3. Close-up of part of the closed singular cycle Γ^0 for case (ii). The segment \overline{Q}^1 lies on the sphere S_w^2 (5.5) of the blowup of \hat{q} defined through (5.3). The segments $\overline{Q}^{2,-}$ and \overline{Q}^4 are vertical (purely in the \hat{y} -direction) whereas the segment \overline{Q}^3 is only visible in the chart $\bar{y} = -1$ (3.9) of (3.7). See Appendix A.7.2. The segment \overline{Q}^5 lies on \overline{L}_a : the extension of S_a onto the blowup cylinder. The connection from U to \hat{F} is shown in Fig. 5.1.

Proof. We describe the mapping \mathcal{L}_ϵ in terms of the blowup (5.3) and the desingularized vector-field \tilde{X} (5.11) using the charts $\kappa_{1,2,3}$ in (5.6), (5.7) and (5.8). The details are delayed to Appendix A. \square

REMARK 5.6. Note that Proposition 5.5 is a local result, independent of assumption (A). It therefore implies, as a corollary, that if V is any compact set contained within the funnel which satisfies $\gamma^w(0) \notin V$, then the forward flow of V leaves the two-fold by following the forward orbit U associated with the visible fold for $\epsilon \ll 1$. This PWS orbit is therefore distinguished among all the forward candidates through the two-fold.

6. Proof of Theorem 4.1. From Proposition 5.4 and Proposition 5.5 it follows that \mathcal{P}_ϵ is well-defined and a contraction on Υ for $\epsilon \ll 1$. By the contraction mapping theorem this provides the existence of a unique attracting fixed point. This gives rise to the limit cycle Γ^ϵ in Theorem 4.1. The properties of Γ^ϵ in Theorem 4.1 follow from the proof of Proposition 5.5 in Appendix A. This then completes the proof of Theorem 4.1.

7. Numerics. In this section we illustrate our main result, Theorem 4.1, with some numerical results, in particular highlighting the differences between the two cases (i) (see Fig. 5.2) and (ii) (see Fig. 5.3). We also perform a partial investigation of the bifurcation of the limit cycles at resonances $\xi = n \in \mathbb{N}$. We consider a simple model made up of a flow for $\hat{y} \leq 1$ (7.1) and an explicit map \mathcal{O} , see (7.6) below, from

$\{\hat{y} = 1\}$ to $\{\hat{y} = -1\}$ to model U and D in assumption (A).

For $\hat{y} \leq 1$, we consider the following system:

$$\begin{aligned} \dot{x} &= \epsilon (|\beta|^{-1}c(1 + \phi(\hat{y})) - (1 - \phi(\hat{y}))), \\ \dot{\hat{y}} &= bz(1 + \phi(\hat{y})) - |\beta|x(1 - \phi(\hat{y})), \\ \dot{z} &= \epsilon (1 + \phi(\hat{y}) + b^{-1}\gamma(1 - \phi(\hat{y}))), \end{aligned} \quad (7.1)$$

with the following parameters (also used in [15]):

$$c - \gamma = \frac{5}{2}, \quad c + \gamma = \frac{3(\xi + 1)}{2(\xi - 1)}, \quad b = 1, \quad \beta = -1, \quad (7.2)$$

giving

$$\lambda_+ = -\frac{3}{2(\xi - 1)}, \quad \lambda_- = \xi\lambda_+, \quad \chi_+ = -2, \quad \chi_- = -\frac{1}{2}, \quad (7.3)$$

and

$$z_1^* = 2 - \frac{\xi - 4}{\xi - 1} > 0,$$

cf. (2.20) and (2.18) for $\xi > 1$. Note that (7.1) is just (3.10) with all \mathcal{O} -terms ignored. We will base our computations on the following C^1 Sotomayor and Teixeira regularization function given in (3.3):

$$\phi(\hat{y}) = -\frac{1}{2}\hat{y}^3 + \frac{3}{2}\hat{y} \quad \text{for } \hat{y} \in (-1, 1) \quad \text{and} \quad \phi(\hat{y}) = \pm 1 \quad \text{for } \hat{y} \gtrless \pm 1,$$

and fix

$$\epsilon = 0.0025.$$

The weak canard of (7.1) is known explicitly:

$$\gamma^w : \quad \hat{y} = \phi^{-1}(-1/3) \approx -0.2261, \quad z = 2x, \quad x \in \mathbb{R}, \quad (7.4)$$

using (7.3), and it is constant with respect to parameters ϵ and ξ . Assumption (B) of section 4 is therefore easy to verify. Similarly, the strong canard is

$$\gamma^s : \quad \hat{y} = \phi^{-1}(1/3) = -\phi^{-1}(-1/3) \approx 0.2261, \quad z = \frac{1}{2}x, \quad x \in \mathbb{R}, \quad (7.5)$$

which is also independent of ϵ and ξ . We then fix the global return mechanism by considering the linear model

$$\widehat{\mathcal{O}} : \{(x, \hat{y}, z) | \hat{y} = 1\} \rightarrow \{(x_+, \hat{y}, z_+) | \hat{y} = -1\} : \quad \begin{pmatrix} x_+ \\ z_+ \end{pmatrix} = \begin{pmatrix} d_x \\ d_z \end{pmatrix} + \frac{1}{2} \begin{pmatrix} 1 & -1 \\ 1 & 1 \end{pmatrix} \begin{pmatrix} x \\ z \end{pmatrix}. \quad (7.6)$$

Essentially this mapping corresponds to \mathcal{G}_ϵ (5.12). We will consider two cases of $d = (d_x, 0, d_z) \in \Sigma_{sl}^-$ in (7.6):

$$\text{Case (1)} : \quad d_x = d_z = -3, \quad (7.7)$$

$$\text{Case (2)} : \quad d_x = -1, \quad d_z = -4. \quad (7.8)$$

Cf. (7.4) and (7.5) case (1) here corresponds to F between γ^w and γ^s while case (2) corresponds to F between l^- and γ^w . Using Definition 5.2 we therefore conclude the following:

LEMMA 7.1. *Suppose $\xi \in (n, n + 1)$. Then*

- *For n odd:*
 - *Case (1) \Rightarrow case (ii).*

- Case (2) \Rightarrow case (i).
- For n even:
 - Case (1) \Rightarrow case (i).
 - Case (2) \Rightarrow case (ii).

Let Ψ_t denote the flow-map of (7.1). Then we obtain the limit cycles Γ^ϵ as fixed points of the return mapping: $\mathcal{P}_\epsilon : \widehat{\Upsilon} \rightarrow \widehat{\Upsilon}$, which we here write as

$$\mathcal{P}_\epsilon(x, z) = (\Psi_{T(x,z)} \circ \widehat{\mathcal{O}})(x, 1, z),$$

with $T(x, z) > 0$ the smallest number so that $\Psi_{T(x,z)}(x, -1, z) \in \{\hat{y} = 1\}$. The limit cycle Γ^ϵ of Theorem 4.1 intersects $\{\hat{y} = -1\}$ around $(x, \hat{y}, z) = (d_x, -1, d_z)$ in a point which we shall denote by

$$(d_x^\epsilon, -1, d_z^\epsilon).$$

We will use d_x^ϵ as a measure of the amplitude. In Fig. 7.1 we show the result of computing limit cycles for case (1) as fixed points of \mathcal{P}_ϵ . We use shooting with MATLAB ode23s to approximate \mathcal{P}_ϵ and apply standard arc-length continuation in ξ . Fig. 7.1(a) shows a bifurcation diagram in the (ξ, d_x^ϵ) -plane. Here:

- The dotted lines are used to indicate limit cycles that intersect $\hat{y} = -1$ near $x = z = 0$.

This corresponds to the case illustrated in Fig. 5.3 for $\epsilon \rightarrow 0$.

- Full lines, on the other hand, correspond to limit cycles that *do not* intersect $\hat{y} = -1$.

This corresponds to the case illustrated in Fig. 5.2 for $\epsilon \rightarrow 0$.

Fig. 7.1(b) shows a zoom of the bifurcation diagram in Fig. 7.1(a) around $\xi = 2$. Two saddle-node bifurcations are visible within this zoom.

The numerical simulations of (7.1) in [15, Section 8, Figs. 9-10] show that only odd values of $\xi > 1$ give rise to secondary canards. This is in line with results on folded nodes in classical slow-fast systems [25]. Therefore it is reasonable to believe that the computed limit cycles interact with the secondary canard around $\xi = 3$ in Fig. 7.1(a). We believe that this is why there is a break in the curve there; our model does not include a global mechanism for the secondary canard to return to the funnel and create a canard-like explosion. But even using high precision numerics we did not manage to connect the curves on either side of $\xi = 4$, even though there is no new additional canard around this value. Presumably the curve around $\xi = 4$ looks like that around $\xi = 2$ but because the curve is so steep we did not manage to resolve this.

Nevertheless, the results shown in Fig. 7.1(a) are in agreement with Theorem 4.1 and the different singular cycles illustrated in Fig. 5.2 and Fig. 5.3. To see this, consider first $\xi \in (n, n+1)$ for $n = 1$ or $n = 3$. According to Lemma 7.1, case (1) then corresponds to case (ii). This agrees with the use of dotted lines in Fig. 7.1. A limit cycle in case (1) for $\xi = 1.5$ is shown in Fig. 7.2(a),(b) using projections onto the (x, \hat{y}) and (z, x) -plane. It is seen how the curve intersects $\hat{y} = -1$ twice around $x = z = 0$ before reaching $\hat{y} = 1$. For $\xi \in (n, n+1)$ with $n = 2$ and $n = 4$ it also follows from Lemma 7.1 that case (1) corresponds to case (i). This agrees with the use of full lines in Fig. 7.1. A limit cycle in case (1) for $\xi = 2.5$ is shown in Fig. 7.2(c),(d).

Fig. 7.2(e),(f) shows a limit cycle in case (2) for $\xi = 1.5$. From Lemma 7.1 this corresponds to case (i). In comparison with case (1) for the same value of $\xi = 1.5$, this case corresponds to being on the other side of the weak canard. In Fig. 7.2(e),(f) we therefore see that the limit cycle does not intersect $\hat{y} = -1$ around $x = z = 0$, in contrast to Fig. 7.2(a),(b). Instead it follows a vertical fiber directly to $\hat{y} = 1$ without the additional twist.

8. Conclusions. PWS systems contain a number of phenomena that have no counterparts in smooth systems. Perhaps one of the most intriguing is the two-fold singularity. Using the Filippov convention, this geometric object contains regions of stable and unstable sliding, arranged in such a way that they meet at only one point, leading to an ambiguity in the forward evolution of the flow there. Not only that, but the two-fold comes in three different flavors; visible, visible-invisible and invisible. Previous work in this resolution of this ambiguity has been mixed. On the one hand, Simpson [21] has shown that, for the visible two-fold in \mathbb{R}^2 , the possibility of evolution through the singularity into the escaping region for a nonzero length of time can be excluded. He also made the point that the regularization of two-folds may turn out to be futile in the absence of further information about the problem. Conversely, in [5], the authors asserted that forward evolution through the singularity into the region of unstable sliding was possible for the invisible two-fold in \mathbb{R}^3 . Such claims were not made for the visible two-fold, nor for the visible-invisible two-fold.

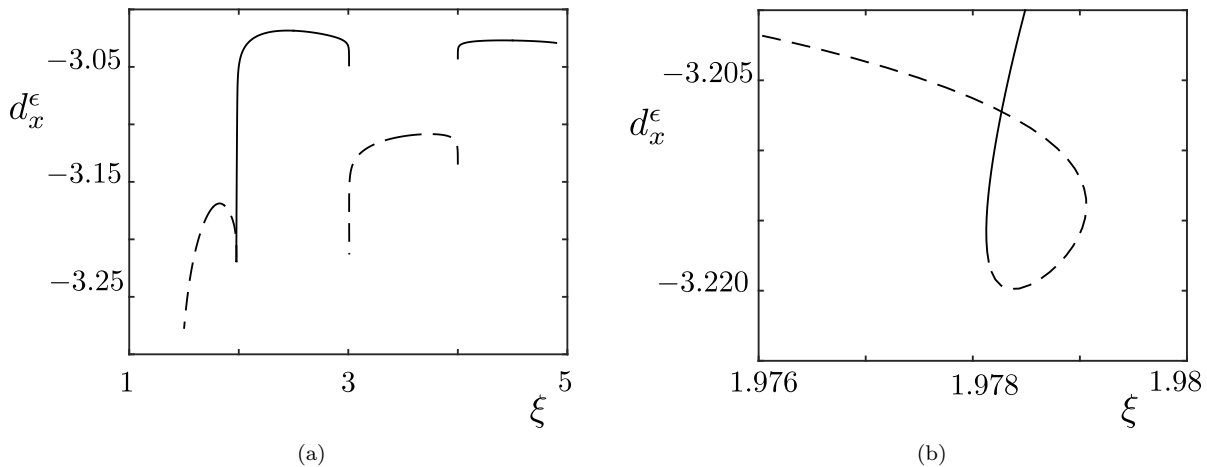


FIGURE 7.1. Bifurcation diagram in the plane (ξ, d_x^ϵ) of limit cycles of the model described by (7.1) and (7.6) in case (1) (7.7). The dotted lines are used to indicate limit cycles that intersect $\hat{y} = -1$ near $x = z = 0$. Full lines, on the other hand, correspond to limit cycles that do not intersect $\hat{y} = -1$. A zoom of the bifurcation diagram in (a) around $\xi = 2$ is shown in (b). It shows two fold points.

In this paper, we use regularization to shed light on the dynamics around the visible-invisible two-fold in \mathbb{R}^3 . Under the mild assumption of the existence of a closed PWS singular cycle through the two-fold (together with non-degeneracy conditions), our main result Theorem 4.1 shows that the Sotomayor and Teixeira regularization of the PWS visible-invisible two-fold possesses a limit cycle that attracts a large set of initial conditions. The PWS singular cycle Γ gives rise to a singular cycle Γ^0 of the regularized system, which has two different cases illustrated in Fig. 5.2 and Fig. 5.3. These cases are carefully analyzed using the blowup method in the formulation of Krupa and Szmolyan (see Appendix A for the details) and illustrated numerically.

As a corollary to Theorem 4.1, see Proposition 5.5 and Remark 5.6, we find that almost all initial conditions within the stable sliding region leave the two-fold by following the forward orbit associated with the visible fold. This orbit is therefore distinguished among all the forward candidates through the two-fold.

In this paper we have considered the simplest possible geometry where Γ consists of just three segments, see assumption (A) in section 4. But the result applies to more complicated singular cycles Γ with several crossing segments. Using the result [15, Theorem 6.2], our approach could also be used to consider a segment ending up at a visible fold. Furthermore, we believe that our results are true for a class of regularization functions more general than those considered in this manuscript. In future work we aim to consider the invisible two-fold. This represents a different type of challenge, since there is no (direct) mechanism to take us away from the two-fold.

The geometry of Fig. 4.1 has similarities with the geometry associated with the folded node in slow-fast system considered in [4]. Our main result, Theorem 4.1, is also similar to [4, Theorem 4.1] where the authors show that the folded node, together with a return mechanism satisfying conditions similar to (B) and (C), gives rise to limit cycles (mixed-mode oscillations) for ϵ sufficiently small. Our work therefore further strengthens the connection between PWS bifurcations and slow-fast phenomena. But there remain significant differences between our work and that of [4]: the slow-fast geometry is truly different (compare Fig. 3.2 with [23, Fig. 2]), their result does not translate directly into our setting and the proof of [4, Theorem 4.1] is only sketched. In addition, the authors do not describe the details of the different scenarios corresponding to cases (i) and (ii). These differences have been illustrated and analyzed numerically in a model of pituitary lactotroph model [24, see e.g. Figs. 12 and 13]. We believe that our approach can be used to provide a complete proof of [4, Theorem 4.1].

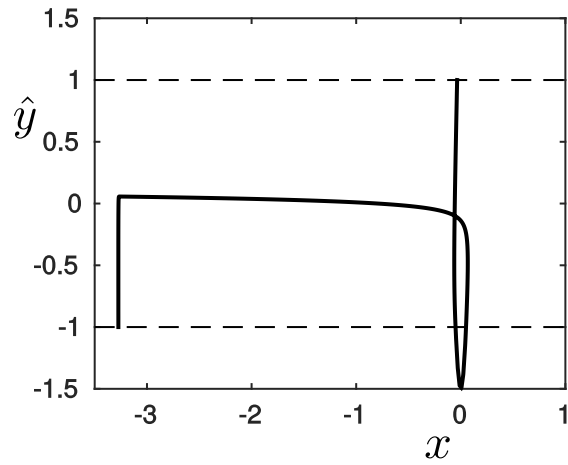
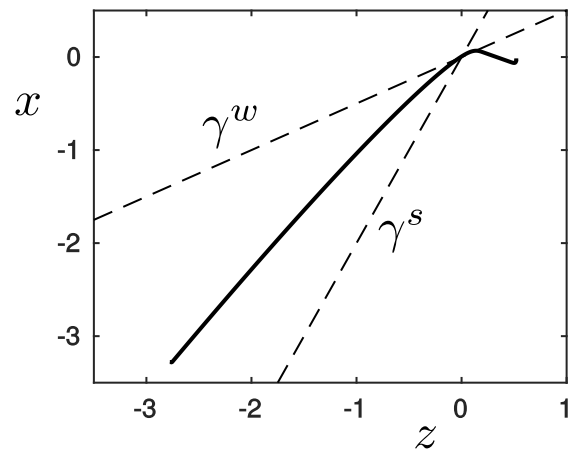
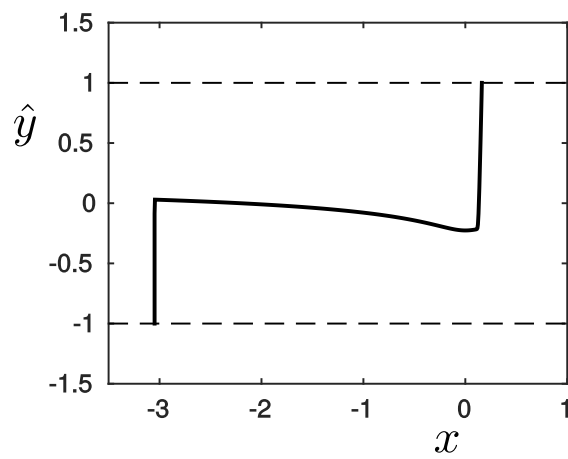
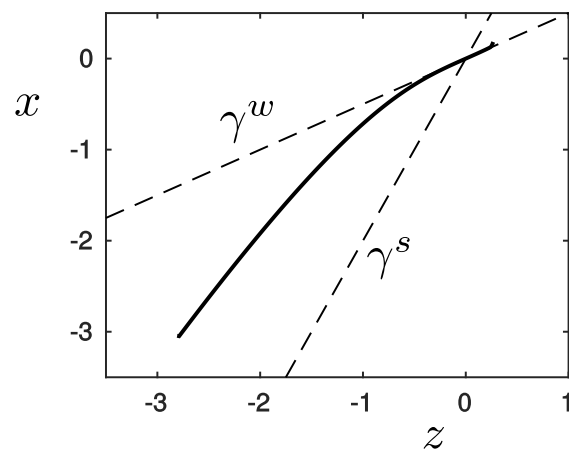
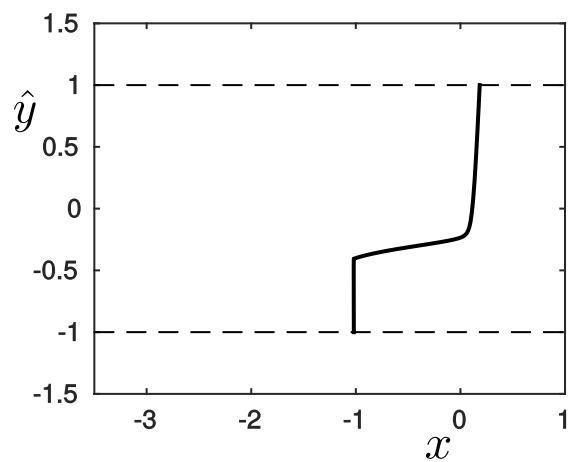
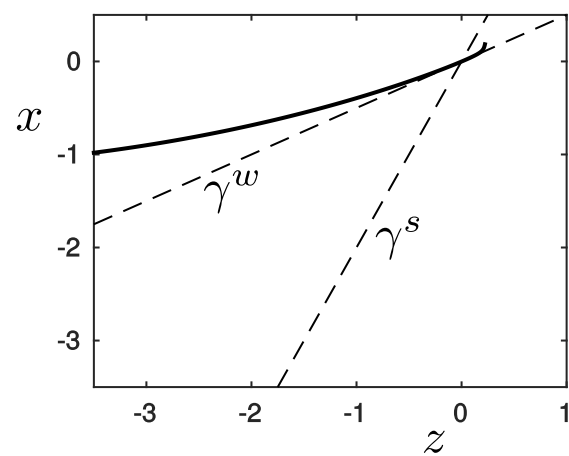
(a) Case (1), $\xi = 1.5$ (b) Case (1), $\xi = 1.5$ (c) Case (1), $\xi = 2.5$ (d) Case (1), $\xi = 2.5$ (e) Case (2), $\xi = 1.5$ (f) Case (2), $\xi = 1.5$

FIGURE 7.2. Limit cycles of (7.1) and (7.6). Cases (1) and (2) are defined in (7.7) and (7.8).

Appendix A. Proof of Proposition 5.5. We describe the mapping \mathcal{L}_ϵ in terms of the blowup (5.3) and the desingularized vector-field \tilde{X} (5.11). We rely on results in Appendix B and detailed estimates in Appendix C.

A.1. Chart κ_1 . Using chart κ_1 we gain hyperbolicity of S_a on the blowup sphere $r_1 = 0$ for $\epsilon_1 = 0$. This gives rise to an extension of the critical manifold $S_{a,1} = \kappa_1(S_a)$ onto the sphere $r_1 = 0$ as a unique attracting critical manifold $C_{a,1}$ for $\epsilon_1 \leq \nu$ with ν sufficiently small. See [15] and Proposition B.1 below. This in turn, by center manifold theory, provides an extension of Fenichel's slow manifold $S_{a,\epsilon}$ as a perturbation of \bar{C}_a up until

$$\Lambda^- : x = -\nu^{-1/2}\sqrt{\epsilon},$$

for ϵ sufficiently small, upon blowing back down. At

$$\Lambda_2^- = \kappa_2(\Lambda^-) : x_2 = -\nu^{-1/2},$$

in chart κ_2 the manifold $S_{a,\epsilon,2} = \kappa_2(S_{a,\epsilon})$ is $\mathcal{O}(\sqrt{\epsilon})$ -close to $C_{a,2} = \kappa_{2,1}(C_{a,1})$.

The blowup splits the strong and weak canards within the reduced problem $S_{a,1} \subset \{\epsilon_1 = 0\}$ through the presence of a saddle (B.7) and a stable node $p_{a,1} \subset \{r_1 = \epsilon_1 = 0\}$ (B.8). Within $C_{a,1}$ the point $p_{a,1}$ is, on the other hand, a saddle with a one-dimensional unstable manifold Q_1^1 . This manifold will extend by the forward flow across the blowup sphere to form $\bar{Q}^1 \in S_w^2$. Recall Fig. 5.2 and Fig. 5.3. The orbit \bar{Q}^1 corresponds to $\bar{\gamma}^w \cap \{r = 0\}$ for $\epsilon = 0$. We illustrate the findings in Fig. A.1.

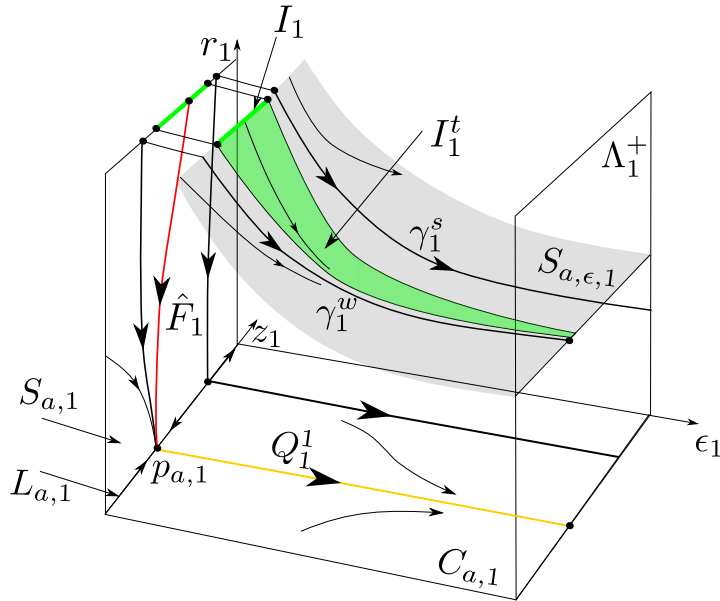


FIGURE A.1. Illustration of the dynamics on the continuation of Fenichel's slow manifold $S_{a,\epsilon,1}$.

A.2. Reduction of \mathcal{L}_ϵ and some notation. The uniform contraction towards $S_{a,\epsilon}$ in chart κ_1 allows us to restrict the description of \mathcal{L}_ϵ to $S_{a,\epsilon}$. The $\mathcal{O}(e^{-c/\epsilon})$ -terms will not be important here. The mapping is therefore just one-dimensional and can be described by $z \in I$ only. We frequently use I to refer to the graph

$$\text{graph}(h_a|_{\{-\rho\} \times I}), \quad (\text{A.1})$$

rather than the interval itself. This approach was already used in Fig. 5.2. It should be clear from the context how I is understood.

We will denote the forward flow of I (as the graph (A.1)) by

$$I^t = \{\phi_t(x, y, z) \mid (x, y, z) \in \text{graph}(h_a|_{\{-\rho\} \times I}), t \geq 0\}.$$

Here we consider $\phi_t(x, y, z)$ as the flow of X_ϵ for $y \leq \epsilon$ (since we only wish to describe the first return to $\Upsilon \subset \{y = \epsilon\}$). To prove Proposition 5.5 we will then study $\mathcal{L}_\epsilon : z \in I \rightarrow I^t \cap \Upsilon$.

A.3. Chart κ_3 . The analysis in chart κ_3 is similar to the analysis in chart κ_1 . We obtain an extension of the critical manifold $S_{r,3} = \kappa_3(S_r)$ onto the sphere $r_3 = 0$ as a unique repelling critical manifold $C_{r,3}$ for $\epsilon_3 \leq \nu$ with ν sufficiently small. By center manifold theory this in turn leads to an extension of Fenichel's slow manifold $S_{r,\epsilon}$ as a perturbation of \bar{C}_r up until

$$\Lambda^+ : x = \nu^{-1}\sqrt{\epsilon},$$

for ϵ sufficiently small. The blowup again splits strong and weak canards within the reduced problem on $S_{a,3} \subset \{\epsilon_3 = 0\}$, now through the presence of a saddle (B.16) and an unstable node:

$$p_{r,3} : (r_3, \hat{y}, z_3, \epsilon_3) = (0, \hat{y}_w, -\chi_+, 0). \quad (\text{A.2})$$

Within $C_{r,3} \subset \{r_3 = 0\}$ the point $p_{r,3}$ is a saddle (upon desingularization) with a one-dimensional stable manifold Q_3^1 . The strong unstable manifold through $p_{r,3}$ (A.2) is

$$W^u(p_{r,3}) : r_3 = 0, \hat{y} \in \mathbb{R}, z_3 = -\chi_+, \epsilon_3 = 0,$$

which intersects $\hat{y} = \pm 1$ in the points

$$q_3^\pm : (r_3, \hat{y}, z_3, \epsilon_3) = (0, \pm 1, -\chi_+, 0), \quad (\text{A.3})$$

respectively. Let

$$Q_3^{2,\pm} = W^u(p_{r,3}) \cap \{\hat{y} \gtrless \hat{y}_w\}. \quad (\text{A.4})$$

See Fig. A.2 below. At

$$\Lambda_2^+ = \kappa_2(\Lambda^+) : x_2 = \nu^{-1/2},$$

in chart κ_2 the manifold $S_{r,\epsilon,2} = \kappa_2(S_{r,\epsilon})$ is $\mathcal{O}(\sqrt{\epsilon})$ -close to $C_{r,2} = \kappa_{2,3}(C_{r,3})$.

A.4. Chart κ_2 . Writing the regularized system (3.10) in chart κ_2 (5.7) gives the following set of equations, setting $r_2 = \sqrt{\epsilon} = 0$:

$$\begin{aligned} \dot{x}_2 &= |\beta|^{-1}c(1 + \phi(\hat{y})) - (1 - \phi(\hat{y})), \\ \dot{\hat{y}} &= bz_2(1 + \phi(\hat{y})) - |\beta|x_2(1 - \phi(\hat{y})), \\ \dot{z}_2 &= 1 + \phi(\hat{y}) + b^{-1}\gamma(1 - \phi(\hat{y})), \end{aligned} \quad (\text{A.5})$$

In this chart $\bar{Q}^1 \subset S_w^2$ takes the following form

$$Q_2^1 : (x_2, \hat{y}, z_2, r_2) = (x_2, \hat{y}_w, -\chi_+x_2, 0), \quad x_2 \in \mathbb{R}, \quad (\text{A.6})$$

with \hat{y}_w as in (5.2). The line Q_2^1 is contained within $C_{a,2} = \kappa_{21}(C_{a,1})$ for $x_2 \leq -\nu^{-1}$ and $C_{r,2} = \kappa_{23}(C_{r,3})$ for $x_2 \geq \nu^{-1}$. We now describe how the tangent spaces of $TC_{a,2}$ twist upon forward flow application of the variation of (A.5) along Q_2^1 . For this we first replace time by x_2 by dividing the equations for \hat{y} and z_2 by \dot{x}_2 and then linearize about the solution

$$(\hat{y}(x_2), z_2(x_2)) = (\hat{y}_w, -\chi_+x_2),$$

corresponding to Q_2^1 . This gives the following set of variational equations:

$$\begin{aligned} \frac{du}{dx_2} &= -\lambda_+^{-1}|\beta|(\psi ux_2 + bv) \\ \frac{dv}{dx_2} &= -b^{-1}\lambda_+^{-1}\lambda_- \psi u. \end{aligned} \quad (\text{A.7})$$

Here we have used the following relations

$$\lambda_+ = -c - b\chi_+, \quad \lambda_- = b\chi_+ - \gamma, \quad (\text{A.8})$$

which follow from (2.14) and (2.17) and defined

$$\psi \equiv \frac{1}{2}|\beta|(1 - |\beta|^{-1}b\chi_+)^2\phi' \left(\frac{1 + |\beta|^{-1}b\chi_+}{1 - |\beta|^{-1}b\chi_+} \right).$$

Notice that $\psi > 0$. Then following [15], (A.7) can be written as a Weber equation

$$\frac{d^2v}{d\bar{x}_2} - \bar{x}_2 \frac{dv}{d\bar{x}_2} + \xi v = 0, \quad (\text{A.9})$$

by replacing x_2 by

$$\bar{x}_2 = (-\psi|\beta|\lambda_+^{-1})^{1/2}x_2,$$

and eliminating u .

LEMMA A.1. *Suppose (B) so that $n < \xi < n + 1$ for $n = \lfloor \xi \rfloor$. Consider the tangent space:*

$$T_{in} \equiv T_{Q_2^1 \cap \Lambda_2^-} C_{a,2}.$$

Then $T_{in} = TQ_2^1 \oplus \text{span}\{\varpi_{in}(\nu)\}$ where

$$\varpi_{in}(\nu) = \left(0, \frac{2\sqrt{\nu}|\beta|^{-1}b}{(1 - |\beta|^{-1}b\chi_+)\phi' \left(\frac{1 + |\beta|^{-1}b\chi_+}{1 - |\beta|^{-1}b\chi_+} \right)} + \mathcal{O}(\nu), 1 \right). \quad (\text{A.10})$$

Under the flow of the variational equations (A.7), the vector ϖ_{in} , is transformed to a tangent vector $\varpi_{out} \in T_{Q_2^1 \cap \Lambda_2^+} C_{a,2}$, based at $\Lambda_2^+ : x_2 = \nu^{-1/2}$, which is transverse to $C_{r,2}$ and satisfies

$$\bar{\varpi}_{out} \equiv \frac{\varpi_{out}(\nu)}{|\varpi_{out}(\nu)|} = (0, \zeta + o(1), o(1)), \quad (\text{A.11})$$

as $\nu \rightarrow 0$, where

$$\zeta = \begin{cases} -1 & \text{if } n \text{ is odd} \\ 1 & \text{if } n \text{ is even} \end{cases} \quad (\text{A.12})$$

Proof. The form of ϖ_{in} is obtained by transforming $C_{a,1}$ (see Proposition B.1 below) into κ_2 :

$$C_{a,2} \equiv \kappa_{21}(C_{a,1}) : \quad \hat{y} = \phi^{-1} \left(\frac{1 - |\beta|^{-1}bx_2^{-1}z_2}{1 + |\beta|^{-1}bx_2^{-1}z_2} \right) + \mathcal{O}(x_2^{-1}),$$

valid for $x_2 \leq -\nu^{-1/2}$. Differentiating this expression with respect to z_2 gives (A.10). The Weber equation (A.9) for $\xi \notin \mathbb{N}$ has two unique linearly independent solutions $v_1(\bar{x}_2)$ and $v_2 = v_1(-\bar{x}_2)$, which are only algebraic in the past and future, respectively. The solution v_1 has exponential growth for $\bar{x}_2 \rightarrow \infty$. Furthermore, $v_1'(\bar{x}_2)$ possesses precisely n roots. Using (A.7) it follows that u also possesses n roots. The solution $v_1(\bar{x}_2)$ corresponds to initial conditions contained within $TC_{a,2}$ (algebraic in the past). Since u in (A.10) is positive at $\Lambda_2^- : x_2 = -\nu^{-1/2}$ (recall $\chi_+ < 0$), the result therefore follows by the number of sign-changes. \square

This lemma establishes the transverse intersection of $C_{a,2}$ with $C_{r,2}$ along Q_2^1 . (This gives rise to the weak canard $\gamma^w(\epsilon)$ for ϵ sufficiently small using the fact that the continuation of $S_{a,\epsilon}$ and $S_{r,\epsilon}$ are $\sqrt{\epsilon}$ -close to $C_{a,2}$ and $C_{r,2}$ at Λ_2^\pm , respectively, see [15].) But furthermore, it allows us to separate the cases (i) and (ii) (see Definition 5.2) dynamically as $\epsilon \rightarrow 0$.

A.5. Combining the results obtained in the charts $\kappa_{1,2,3}$. The compact interval I (or more precisely the graph of $h_a|_{\{-\rho\} \times I}$) in section 5.3 is by assumption (C) contained within the funnel but is bounded away from $\gamma^w(0)$. Therefore it can be (a) between l^- and $\gamma^w(0)$ or (b) between $\gamma^w(0)$ and $\gamma^s(0)$. The scenario illustrated in Fig. 4.1 corresponds to (b). Upon passage through chart κ_1 , I_1^t contracts towards $\gamma_2^w(\epsilon)$ at $\Lambda_2^- : x_2 = -\nu^{-1}$ for $\epsilon \ll 1$. See Lemma C.1. The contraction occurs along directions which can be approximated by the tangent spaces $TC_{a,2}$ and in particular T_{in} in Lemma A.1. Here (a) corresponds to contraction along the positive direction of $\varpi_{in}(\nu)$ whereas (b) corresponds to contraction along the negative direction of $\varpi_{in}(\nu)$.

A.6. Case (i). Using Lemma A.1 and (A.11) we therefore realize in case (i) that I_2^t is *above* the extended slow manifold $S_{r,\epsilon,2} = \kappa_2(S_{r,\epsilon})$ at $\Lambda_2^+ : x_2 = \nu^{-1}$ for $\epsilon \ll 1$. See Fig. A.2 (a). Using the repulsion from the repelling manifold $S_{r,\epsilon}$ in chart κ_3 we can therefore conclude in Lemma C.3 and Lemma C.4 that the set I_3^t follows (and converges to as $\epsilon \rightarrow 0$) the union of Q_3^1 and the vertical fiber $Q_3^{2,+}$ of the base point $p_{r,3}$ on $C_{r,3}$ upwards until $\hat{Y} \subset \{\hat{y} = 1\}$. See Fig. A.2 (a). The contraction in chart κ_1 establishes the desired result on \mathcal{L}_ϵ in Proposition 5.5 for case (i).

A.7. Case (ii). In this case I_2^t is *below* the extended slow manifold $S_{r,\epsilon,2} = \kappa_2(S_{r,\epsilon})$ at $\Lambda_2^+ : x_2 = \nu^{-1}$ for $\epsilon \ll 1$. See Fig. A.2 (b). In Lemma C.3 and Lemma C.4 we therefore conclude in chart κ_3 that I_3^t follows (and converges to as $\epsilon \rightarrow 0$) the union of Q_3^1 and the vertical fiber $Q_3^{2,-}$ of the base point $p_{r,3}$ on $C_{r,3}$ downwards $\hat{y} \leq \hat{y}_w$. See Fig. A.2 (b). In particular, $Q_3^{2,-}$ intersects $\{\hat{y} = -1\}$ in

$$q_3^- : r_3 = 0, \hat{y} = -1, z_3 = -\chi_+, \epsilon_3 = 0.$$

The vector-field X^- has an invisible fold at $l^- : x = y = 0$ and the flow of X^- therefore defines a mapping from $\Sigma_{sl}^+ \subset \{y = 0, x > 0\}$ to $\Sigma \cap \{x < 0\}$. Recall Proposition 2.6. This establishes a return of I^t to $\{\hat{y} = -1\}$. But in chart $\bar{\epsilon} = 1$ of (3.7) the PWS system is not observable for $\epsilon = 0$. There are two approaches to overcome this difficulty:

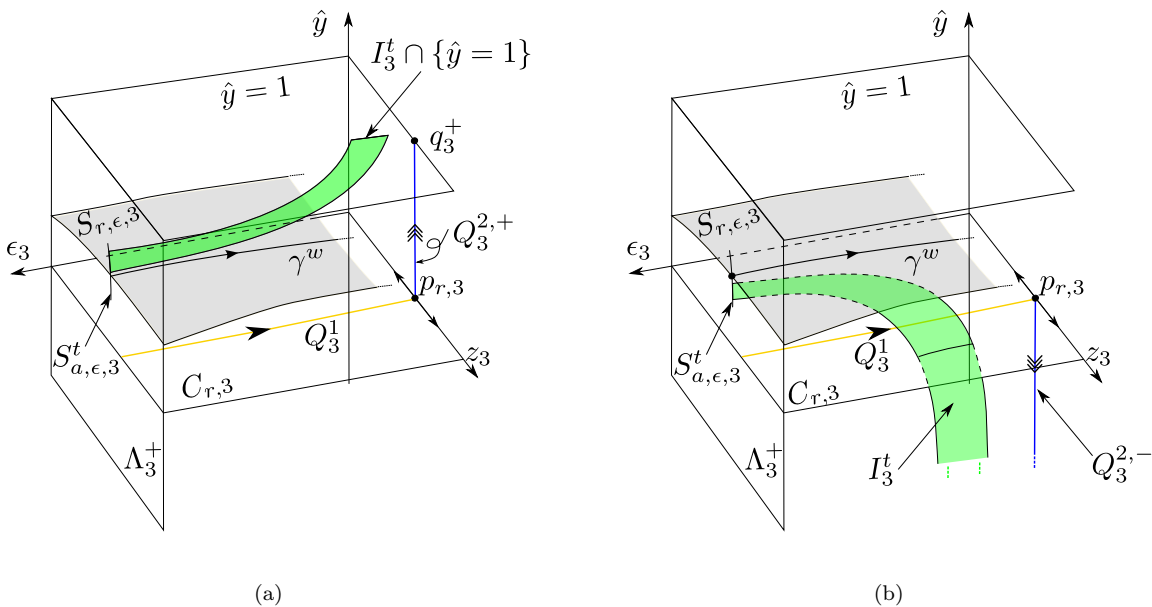


FIGURE A.2. Illustration of the dynamics in chart κ_3 using a projection onto the $(\epsilon_3, z_3, \hat{y})$ -space. (a) corresponds to case (i). (b) corresponds to case (ii). Here $S_{a,\epsilon,3}^t$ is the forward flow of $S_{a,\epsilon,1}$.

A.7.1. The direct approach. The first approach is to exploit the finite deformation 1° in Definition 3.1 and compute a mapping σ_ϵ^- from $\{y = -\epsilon\}$ to itself as the forward flow of X^- and then write this mapping in terms of the charts κ_3 and κ_1 . This gives rise to a smooth mapping $\sigma_{3,1}^- : \kappa_3 \cap \{\hat{y} = -1\} \rightarrow \kappa_1 \cap \{\hat{y} = -1\}$

even for $\epsilon = 0$; see Lemma C.5. The application of this mapping to $q_3^- = Q_3^{2,-} \cap \{\hat{y} = -1\}$ gives a point

$$q_1^- : z_1 = z_1^*, r_1 = 0, \epsilon_1 = 0, \hat{y} = -1, \quad (\text{A.13})$$

where

$$z_1^* = -\chi_+ + \frac{2\gamma}{b}, \quad (\text{A.14})$$

which by (2.20) is contained outside of the funnel in chart κ_1 . Recall Proposition 2.6 and Fig. 2.2. $\sigma_{3,1}^-$ maps a neighborhood of q_1^+ onto a neighborhood of q_1^- . This enables the description of $I_1^t \cap \{\hat{y} = -1\}$ in Lemma C.7.

A.7.2. The geometric approach. An alternative, more geometric, approach to describe the return of I^t to $\{y = -\epsilon\}$, is to consider the chart $\bar{y} = -1$ (3.9) of the blowup (3.7). We outline this approach in the following focussing on the singular case $\epsilon = 0$. This approach also generalizes to regularization functions such as \tanh that violate condition 1° in Definition 3.1.

Chart $\bar{y} = -1$. Consider the equations (3.6). From (3.5) it follows that these equations coincide with (2.6) for $y \leq -\epsilon$:

$$\begin{aligned} \dot{x} &= \epsilon(-1 + \mathcal{O}(x + y + z)), \\ \dot{y} &= \epsilon(\alpha y - |\beta|x + \mathcal{O}((x + y)(x + y + z))), \\ \dot{z} &= \epsilon(b^{-1}\gamma + \mathcal{O}(x + y + z)), \\ \dot{\epsilon} &= 0, \end{aligned} \quad (\text{A.15})$$

written here in terms of the fast time $\tau = \epsilon^{-1}t$. We write these equations in the chart $\bar{y} = -1$ (3.9) of (3.7). This gives the following equations:

$$\begin{aligned} \dot{x} &= -y(-1 + \mathcal{O}(x + y + z)), \\ \dot{y} &= yJ(x, y, z, \hat{\epsilon}), \\ \dot{z} &= -y(b^{-1}\gamma + \mathcal{O}(x + y + z)), \\ \dot{\hat{\epsilon}} &= -\hat{\epsilon}J(x, y, z, \hat{\epsilon}), \end{aligned} \quad (\text{A.16})$$

after desingularization through division by $\hat{\epsilon}$ on the right hand side, where

$$J(x, y, z, \hat{\epsilon}) = |\beta|x + \mathcal{O}(y + (x + y)(x + y + z)).$$

The two-fold now becomes

$$\hat{q} : x = y = z = 0, \hat{\epsilon} \geq 0. \quad (\text{A.17})$$

For simplicity we use the same symbol as in chart $\bar{\epsilon} = 1$ in (3.8). We therefore consider the following blowup (reminiscent of (5.3)):

$$x = r\bar{x}, y = r^2\bar{y}, z = r\bar{z}, \quad (\bar{x}, \bar{y}, \bar{z}) \in S^2, \quad (\text{A.18})$$

blowing up the new \hat{q} in (A.17) to a cylinder of spheres $(\hat{\epsilon}, (\bar{x}, \bar{y}, \bar{z})) \in \mathbb{R}_+ \times S^2$. We again desingularize through division by r . Note that $\hat{\epsilon}$ (as \hat{y} in (5.3)) is not transformed by this blowup. We then consider the following charts:

$$\kappa_1 : \bar{x} = -1 : x = -r_1, y = r_1^2 y_1, z = r_1 z_1, \quad (\text{A.19})$$

$$\kappa_2 : \bar{y} = -1 : x = r_2 x_2, y = -r_2^2, z = r_2 z_2,$$

$$\kappa_3 : \bar{x} = 1 : x = r_3, y = r_3^2 y_3, z = r_3 z_3, \quad (\text{A.20})$$

abusing notation slightly by using the same name for the charts as used in relation to (5.3). We consider the charts in Appendix D. But in summary, we obtain \bar{Q}^3 as a heteroclinic connection of the blowup vector-field, connecting the end of $Q_3^{2,-}$:

$$r_3 = 0, y_3 = 0, \epsilon_3 = 0, z_3 = -\chi_+,$$

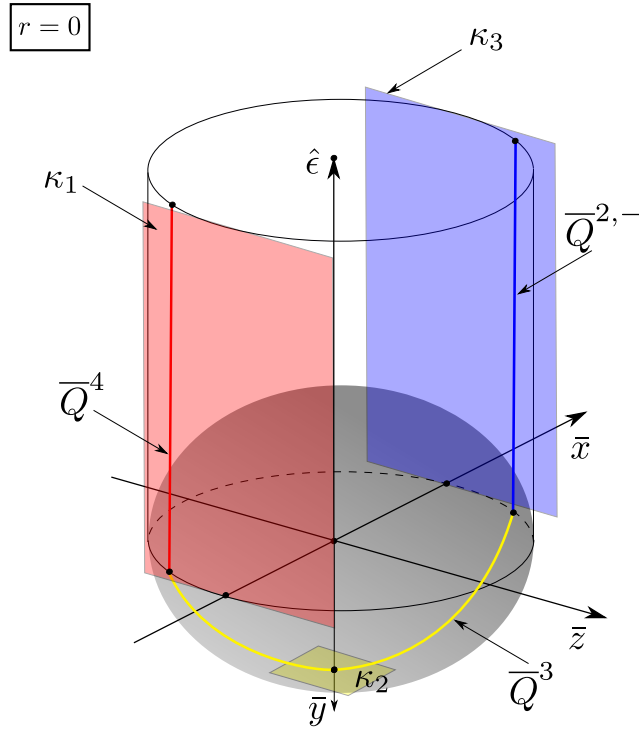


FIGURE A.3. Singular orbit \bar{Q}^3 identified in the chart $\bar{y} = -1$ of blowup (3.7) using the blowup (A.18).

within $\hat{\epsilon} = 0$ of chart κ_3 (A.20), with the point

$$(r_1, y_1, z_1, \hat{\epsilon}) = (0, 0, z_1^*, 0), \quad (\text{A.21})$$

in chart κ_1 (A.19), with z_1^* as in (A.14), in forward time; see Lemma D.1 and Lemma D.2. From (A.21) we obtain

$$Q_1^4: \quad r_1 = y_1 = 0, \quad z_1 = z_1^*, \quad \hat{\epsilon} \geq 0,$$

as the associated unstable manifold; see Lemma D.3. The results are illustrated in Fig. A.3.

A.7.3. Chart κ_1 again. It is possible to follow \bar{Q}^4 back into the chart κ_1 (5.6) of the blowup (5.3). There it becomes

$$Q_1^4: \quad z_1 = z_1^*, \quad r_1 = 0, \quad \epsilon_1 = 0, \quad \hat{y} \leq \hat{y}_*, \quad (\text{A.22})$$

where \hat{y}_* depends on the sign of z_1^* . As expected, Q_1^4 intersects $\{\hat{y} = -1\}$ in q_1^- (A.13).

The case $z_1^* < 0$. In this case the mapping σ_0^- takes points near the weak eigendirection into the region of stable sliding Σ_{sl}^- . Therefore

$$\hat{y}_* = \phi^{-1} \left(\frac{1 + |\beta|^{-1} b z_1^*}{1 - |\beta|^{-1} b z_1^*} \right) \in (-1, 1), \quad (\text{A.23})$$

in (A.13) and the forward flow of q_1^- contracts to the base point on $L_{a,1} = S_{a,1} \cap C_{a,1} \subset \{r_1 = \epsilon_1 = 0\}$:

$$z_1 = z_1^*, \quad r_1 = 0, \quad \epsilon_1 = 0, \quad \hat{y} = \hat{y}_*, \quad (\text{A.24})$$

following Q_1^4 as a stable fiber. Since $z_1^* > \chi_-$ cf. (2.20), the reduced problem on $L_{a,1} = C_{a,1} \cap \{\epsilon_1 = 0\}$ in (B.10) takes (A.24) by the orbit Q_1^5 to

$$q_1^+ : \quad z_1 = 0, \quad r_1 = 0, \quad \epsilon_1 = 0, \quad \hat{y} = 1. \quad (\text{A.25})$$

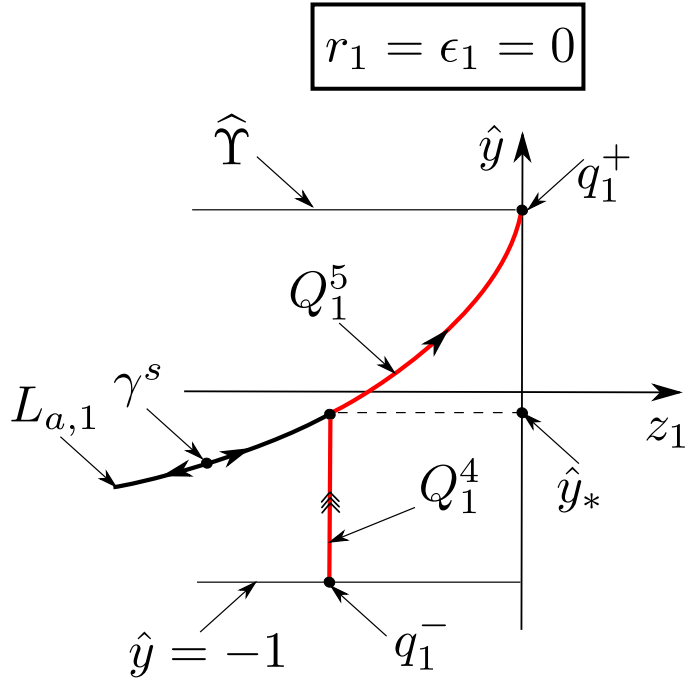


FIGURE A.4. Illustration of q_1^- , Q_1^4 , Q_1^5 and q_1^+ within chart κ_1 and $r_1 = 0$ for $z_1^* < 0$.

See Fig. A.4. But the point

$$q_1^+ : r_1 = 0, \hat{y} = 1, z_1 = 0, \epsilon_1 = 0,$$

is a nonhyperbolic point of (B.1). This is due to the loss of hyperbolicity of \hat{l}^+ (see also Theorem 3.3). So (in principle) a further blowup is required to study this region. We postpone the details of this to Appendix C.4. But in summary, the initial contraction in chart κ_1 towards the weak canard, detailed in Lemma C.1, establishes the desired result on \mathcal{L}_ϵ in Proposition 5.5 for case (ii) $z_1^* < 0$. This completes the proof of Proposition 5.5.

The case $z_1^* > 0$. This case is illustrated for the PWS system in Fig. 2.2. The mapping σ_0^- takes points near the weak eigendirection into the region of crossing upwards Σ_{cr}^+ . Therefore $\hat{y}_* = 1$ in (A.13). In particular, the forward flow in chart κ_1 maps q_1^- directly to (a new)

$$q_1^+ : z_1 = z_1^*, r_1 = 0, \epsilon_1 = 0, \hat{y} = 1,$$

within $\{\hat{y} = 1\}$. This enables a description of $I^t \cap \Upsilon \subset \{y = \epsilon\}$, see Lemma C.10 in Appendix C.5. In summary, the initial contraction in chart κ_1 towards the weak canard, detailed in Lemma C.1, again establishes the desired result in Proposition 5.5. In the exceptional case where $z_1^* = 0$ we also have $\hat{y}_* = 1$. This is analyzed in Appendix C.6 leading to similar conclusions.

Appendix B. Blowup of \hat{q} in chart $\bar{\epsilon} = 1$. In this section we consider the results from [15] on the analysis of the two charts κ_1 and κ_3 used to describe the blowup cylinder of (5.3) in the chart $\bar{\epsilon} = 1$ of (3.7).

B.1. Chart κ_1 . Writing the regularized system (3.10) in chart κ_1 (5.6) gives the following set of equations:

$$\begin{aligned} \dot{r}_1 &= -r_1 \epsilon_1 G_1(r_1, y, z_1, \epsilon_1), \\ \dot{\hat{y}} &= (b + \mathcal{O}(r_1)) z_1 (1 + \phi(\hat{y})) + (|\beta| + \mathcal{O}(r_1)) (1 - \phi(\hat{y})), \\ \dot{z}_1 &= \epsilon_1 ((1 + \mathcal{O}(r_1)) (1 + \phi(\hat{y})) + (b^{-1} \gamma + \mathcal{O}(r_1)) (1 - \phi(\hat{y})) + G_1(r_1, y, z_1, \epsilon_1) z_1), \\ \dot{\epsilon}_1 &= 2G_1(r_1, y, z_1, \epsilon_1) \epsilon_1^2, \end{aligned} \tag{B.1}$$

with

$$G_1(r_1, y, z_1, \epsilon_1) = (|\beta|^{-1} c + \mathcal{O}(r_1)) (1 + \phi(\hat{y})) + (-1 + \mathcal{O}(r_1)) (1 - \phi(\hat{y}))$$

and where we have desingularized by division by r_1 . Here $\{\epsilon_1 = 0\}$ and $\{r_1 = 0\}$ are two invariant sub-spaces. Their intersection is a line of hyperbolic equilibria $L_{a,1}$ determined by

$$L_{a,1} : (r_1, \hat{y}, z_1, \epsilon_1) = \left(0, \phi^{-1} \left(\frac{1 + |\beta|^{-1} b z_1}{1 - |\beta|^{-1} b z_1} \right), z_1, 0 \right), \quad z_1 < 0. \tag{B.2}$$

Consider the set

$$U_1 = \{(r_1, \hat{y}, z_1, \epsilon_1) \mid r_1 \in [0, \rho], \quad -\theta^{-1} \leq z_1 \leq -\theta < 0, \quad \hat{y} \in [-1, 1], \quad \epsilon_1 \in [0, \nu]\},$$

for ρ, θ and ν small. Let

$$\hat{y}_s \equiv \phi^{-1} \left(\frac{1 + |\beta|^{-1} b \chi_-}{1 - |\beta|^{-1} b \chi_-} \right), \quad \hat{y}_w \equiv \phi^{-1} \left(\frac{1 + |\beta|^{-1} b \chi_+}{1 - |\beta|^{-1} b \chi_+} \right).$$

We can then summarize the following properties from [15, Proposition 7.4]:

PROPOSITION B.1. *For ρ, θ and ν sufficiently small the following statements hold true within U_1 :*

- *There exists a 3D attracting center manifold*

$$M_{a,1} : \quad \hat{y} = \phi^{-1} \left(\frac{1 + |\beta|^{-1} b z_1}{1 - |\beta|^{-1} b z_1} \right) + \mathcal{O}(r_1 + \epsilon_1), \tag{B.3}$$

of the set of fixed points $L_{a,1}$ for Eqs. (B.1), which is a graph over r_1, z_1 and ϵ_1 .

- *The center manifold $M_{a,1}$ is foliated by invariant hyperbolas $\epsilon = r_1^2 \epsilon_1$. $M_{a,1} \cap \{\epsilon = r_1^2 \epsilon_1\}$ is $\mathcal{O}(e^{-c/\epsilon})$ -close to the Fenichel slow manifold $S_{a,\epsilon}$ within $\{r_1 = \rho\}$.*
- *$M_{a,1}$ includes $S_{a,1}$ contained within $\epsilon_1 = 0$ as a manifold of equilibria, corresponding to the critical manifold S_a .*
- *$M_{a,1}$ also includes*

$$C_{a,1} : (r_1, \hat{y}, z_1, \epsilon_1) = \left(0, \phi^{-1} \left(\frac{1 + |\beta|^{-1} b z_1}{1 - |\beta|^{-1} b z_1} \right) + \mathcal{O}(\epsilon_1), z_1, \epsilon_1 \right), \tag{B.4}$$

contained within $r_1 = 0$ as a unique center sub-manifold, which contains the invariant lines

$$(r_1, \hat{y}, z_1, \epsilon_1) = (0, \hat{y}_s, \chi_-, \epsilon_1), \quad \epsilon_1 \geq 0, \tag{B.5}$$

and

$$Q_1^1 : (r_1, \hat{y}, z_1, \epsilon_1) = (0, \hat{y}_w, \chi_+, \epsilon_1), \quad \epsilon_1 \geq 0, \tag{B.6}$$

with χ_{\pm} from (2.17).

- The lines (B.5) and (B.6) emanate from the equilibria

$$(r_1, \hat{y}, z_1, \epsilon_1) = (0, \hat{y}_s, \chi_-, 0), \quad (\text{B.7})$$

and

$$p_{a,1} : (r_1, \hat{y}, z_1, \epsilon_1) = (0, \hat{y}_w, \chi_+, 0), \quad (\text{B.8})$$

respectively.

- Near $p_{a,1}$ the center manifold $M_{a,1}$ takes the following form:

$$M_{a,1} : \hat{y} = \phi^{-1} \left(\frac{1 + |\beta|^{-1} b z_1}{1 - |\beta|^{-1} b z_1} \right) + r_1 \psi_0 + \epsilon_1 r_1 \psi_1 + \epsilon_1 (z_1 - \chi_+) \psi_2, \quad (\text{B.9})$$

with

$$\psi_0 = \psi_0(r_1, z_1), \quad \psi_1 = \psi_1(r_1, \epsilon_1), \quad \psi_2 = \psi_2(r_1, z_1, \epsilon_1),$$

smooth.

Proof. See [15] for details. Expression (B.9) is not detailed in [15] but follows easily from Taylor expansions and invariance of the line Q_1^1 . \square

Following this proposition we therefore view $S_{a,\epsilon,1} \equiv M_{a,1} \cap \{\epsilon = r_1^2 \epsilon_1\}$ as an extension of the Fenichel's slow manifold up until

$$\Lambda_1^- : \epsilon_1 = \nu.$$

By blowing back down this provides an extension of $S_{r,\epsilon}$ up until $x = -\nu^{-1} \sqrt{\epsilon}$.

Reduced equations near Q_1^1 . Let

$$\tilde{z}_1 = z_1 - \chi_+.$$

Then $r_1 = \tilde{z}_1 = 0$ corresponds to Q_1^1 within $C_{a,1}$. Furthermore, set

$$\Lambda_1^+ = \{\epsilon_1 = \nu\}.$$

Then on $M_{a,1}$ we obtain the following reduced equations

$$\begin{aligned} r_1' &= -r_1, \\ \tilde{z}_1' &= -(\mu + b\lambda_+^{-1} \tilde{z}_1)(1 - b\lambda_+^{-1} \tilde{z}_1)^{-1} \tilde{z}_1 + r_1 G_0(r_1, \tilde{z}_1) + \epsilon_1 (r_1 G_1(r_1, \epsilon_1) + \tilde{z}_1 G_2(r_1, \tilde{z}_1, \epsilon_1)), \\ \epsilon_1' &= 2\epsilon_1. \end{aligned} \quad (\text{B.10})$$

Here

$$\mu = \xi - 1 > 0, \quad (\text{B.11})$$

where

$$\xi = \lambda_+^{-1} \lambda_-, \quad (\text{B.12})$$

is the ratio of the eigenvalues, which by assumption satisfies $\xi > 1$ (see (2.14) and (2.15)). In obtaining (B.10) we have used (B.1) and (B.9) and divided by $\epsilon_1 G_1$. The linearization about $(0, 0, 0)$ (dropping here the \hat{y} -component) therefore has eigenvalues -1 , $-\mu$ and 2 .

B.2. Chart κ_3 . Writing the regularized system (3.10) in chart κ_3 (5.8) gives the following set of equations:

$$\begin{aligned} \dot{r}_3 &= r_3 \epsilon_3 G_3(r_3, \hat{y}, z_3, \epsilon_3), \\ \dot{\hat{y}} &= (b + \mathcal{O}(r_3))z_3(1 + \phi(\hat{y})) + (-|\beta| + \mathcal{O}(r_3))(1 - \phi(\hat{y})), \\ \dot{z}_3 &= \epsilon_3 ((1 + \mathcal{O}(r_3))(1 + \phi(\hat{y})) + (b^{-1}\gamma + \mathcal{O}(r_3))(1 - \phi(\hat{y})) - G_3(r_3, \hat{y}, z_3, \epsilon_3)z_3), \\ \dot{\epsilon}_3 &= -2G_3(r_3, \hat{y}, z_3, \epsilon_3)\epsilon_3^2, \end{aligned} \tag{B.13}$$

where

$$G_3(r_3, \hat{y}, z_3, \epsilon_3) = (|\beta|^{-1}c + \mathcal{O}(r_3))(1 + \phi(\hat{y})) + (-1 + \mathcal{O}(r_3))(1 - \phi(\hat{y}))$$

and where we have desingularized by division by r_3 . Now we consider the set:

$$U_3 = \{(r_3, \hat{y}, z_3, \epsilon_3) \mid r_3 \in [0, \rho], \quad 0 < \theta \leq z_3 \leq \theta^{-1}, \quad \hat{y} \in [-1, 1], \quad \epsilon_1 \in [0, \nu]\}.$$

We then obtain the following proposition, similar to Proposition B.1 in chart κ_1 :

PROPOSITION B.2. *For ρ , θ and ν sufficiently small the following statements hold true within U_3 :*

- *There exists a 3D repelling center manifold*

$$M_{r,3} : \quad \hat{y} = \phi^{-1} \left(\frac{1 - |\beta|^{-1}bz_3}{1 + |\beta|^{-1}bz_3} \right) + \mathcal{O}(r_3 + \epsilon_3),$$

of the set of fixed points

$$L_{r,3} : \quad r_3 = 0, \quad \hat{y} = \hat{y} = \phi^{-1} \left(\frac{1 - |\beta|^{-1}bz_3}{1 + |\beta|^{-1}bz_3} \right), \quad \epsilon_3 = 0,$$

for Eqs. (B.13), which is a graph over r_3, z_3 and ϵ_3 .

- *The center manifold $M_{r,3}$ is foliated by invariant hyperbolas $\epsilon = r_3^2 \epsilon_3$. $M_{r,3} \cap \{\epsilon = r_3^2 \epsilon_3\}$ is $\mathcal{O}(e^{-c/\epsilon})$ -close to the Fenichel slow manifold $S_{r,\epsilon}$ within $\{r_1 = \rho\}$.*
- *$M_{r,3}$ includes $S_{r,3}$ contained within $\epsilon_3 = 0$ as a manifold of equilibria corresponding to the critical manifold S_r .*
- *$M_{r,3}$ also includes*

$$C_{r,3} : (r_3, \hat{y}, z_3, \epsilon_3) = \left(0, \phi^{-1} \left(\frac{1 - |\beta|^{-1}bz_3}{1 + |\beta|^{-1}bz_3} \right) + \mathcal{O}(\epsilon_3), z_3, \epsilon_3 \right),$$

contained within $r_3 = 0$ as a unique center sub-manifold, which contains the invariant lines

$$r_3 = 0, \quad \hat{y} = \phi^{-1} \left(\frac{1 + |\beta|^{-1}b\chi_-}{1 - |\beta|^{-1}b\chi_-} \right), \quad z_3 = -\chi_-, \quad \epsilon_3 \geq 0. \tag{B.14}$$

and

$$Q_3^1 : \quad r_3 = 0, \quad \hat{y} = \phi^{-1} \left(\frac{1 + |\beta|^{-1}b\chi_+}{1 - |\beta|^{-1}b\chi_+} \right), \quad z_3 = -\chi_+, \quad \epsilon_3 \geq 0. \tag{B.15}$$

- *The lines (B.14) and (B.15) emanate from the points*

$$(r_3, \hat{y}, z_3, \epsilon_3) = (0, \hat{y}_s, -\chi_-, 0). \tag{B.16}$$

and

$$p_{r,3} : (r_3, \hat{y}, z_3, \epsilon_3) = (0, \hat{y}_w, -\chi_+, 0), \tag{B.17}$$

respectively.

- Near $p_{r,3}$ the center manifold $M_{r,3}$ takes the following form:

$$M_{r,3}: \quad \hat{y} = \phi^{-1} \left(\frac{1 - |\beta|^{-1} b z_3}{1 + |\beta|^{-1} b z_3} \right) + r_3 \psi_0 + \epsilon_3 r_3 \psi_1 + \epsilon_1 (z_3 + \chi_+) \psi_2,$$

with

$$\psi_0 = \psi_0(r_3, z_3), \quad \psi_1 = \psi_1(r_3, \epsilon_3), \quad \psi_2 = \psi_2(r_3, z_3, \epsilon_3),$$

smooth.

Following this proposition we therefore view $S_{r,\epsilon,3} \equiv M_{r,3} \cap \{\epsilon = r_3^2 \epsilon_3\}$ as an extension of the Fenichel's slow manifold up until $\epsilon_3 = \nu$. By blowing back down this provides an extension of $S_{r,\epsilon}$ up until $x = \nu^{-1} \sqrt{\epsilon}$.

Normal form. Let $z_3 = -\chi_+ + \tilde{z}_3$ and write $M_{r,3}$ in Proposition B.2 as

$$M_{r,3}: \quad \frac{1 - \phi(\hat{y})}{1 + \phi(\hat{y})} = w_3(r_3, \tilde{z}_3, r_3) \equiv |\beta|^{-1} b (-\chi_+ + \tilde{z}_3) + \mathcal{O}(r_3 + \epsilon_3(r_3 + \tilde{z}_3)). \quad (\text{B.18})$$

Now introduce \tilde{y} as a new dynamic variable measuring the deviation from (B.18) by setting

$$\frac{1 - \phi(\hat{y})}{1 + \phi(\hat{y})} = w_3(r_3, \tilde{z}_3, r_3) - \tilde{y}.$$

Then $M_{r,3} \subset \{\tilde{y} = 0\}$. Note $\frac{\partial \tilde{y}}{\partial \hat{y}} > 0$ since $\frac{d}{d\hat{y}} \left\{ \frac{1 - \phi(\hat{y})}{1 + \phi(\hat{y})} \right\} < 0$.

LEMMA B.3. *Within a sufficiently small neighborhood of $(r_3, \tilde{y}, \tilde{z}_3, \epsilon_3) = 0$ there exists a smooth transformation: $(r_3, \tilde{y}, \tilde{z}_3, \epsilon_3) \mapsto \hat{z}_3$ defined by*

$$\tilde{z}_3 = \hat{z}_3 + \epsilon_3 \tilde{y} H(r_3, \tilde{y}, \hat{z}_3, \epsilon_3), \quad (\text{B.19})$$

so that

$$\dot{r}_3 = r_3 \epsilon_3, \quad (\text{B.20})$$

$$\dot{\hat{z}}_3 = \epsilon_3 \left((1 + \lambda_+^{-1} b \hat{z}_3)^{-1} (\mu - b \lambda_+^{-1} \hat{z}_3) \hat{z}_3 + r_3 G_0(r_3, \hat{z}_3) + \epsilon_3 r_3 G_1(r_3, \epsilon_3) + \epsilon_3 \hat{z}_3 G_2(r_3, \hat{z}_3, \epsilon_3) \right),$$

$$\dot{\epsilon}_3 = -2\epsilon_3^2, \quad (\text{B.21})$$

and

$$\dot{\tilde{y}} = (g_0 + \mathcal{O}(r_3 + \tilde{y} + \hat{z}_3 + \epsilon_3)) \tilde{y}. \quad (\text{B.22})$$

where μ is defined in (B.11) and

$$g_0 \equiv \frac{2|\beta| \phi'(\hat{y})}{(-\lambda_+)(1 + \phi(\hat{y}))^2} > 0 \quad \text{with} \quad \hat{y} = \phi^{-1} \left(\frac{1 + |\beta|^{-1} b \chi_+}{1 - |\beta|^{-1} b \chi_+} \right) \in (-1, 1).$$

Proof. This is obtained by straightening out the smooth fibers, see e.g. [13]. \square

The linearization of $p_{r,3}$ as an equilibrium $(0, 0, 0)$ of the reduced equations (B.20), desingularized through division of ϵ_3 , has eigenvalues 1 , μ and -2 .

Appendix C. Estimates for \mathcal{L}_ϵ . In this section we derive estimates of the forward flow of I, I^t , relevant for the proof of Proposition 5.5.

C.1. Chart κ_1 . We first describe the mapping

$$\{r_1 = \rho\} \supset I_1 \ni \tilde{z}_1 \mapsto \tilde{z}_{1,+}(z_1) \in I_1^t \cap \Lambda_1^+, \quad (\text{C.1})$$

obtained by the forward flow of (B.10) on the invariant set $\epsilon = r_1^2 \epsilon_1$. By assumption on I we have that $\tilde{z}_1 \rightarrow 0$ for $t \rightarrow \infty$ within $\epsilon_1 = 0$. Therefore by reducing ρ somewhat, corresponding to flowing I_1 slightly forward, we may suppose that

$$I_1 \subset \{\tilde{z}_1 \in (-\delta, \delta)\},$$

with δ sufficiently small.

LEMMA C.1. *Fix $\vartheta \in (0, 1)$. Then for ρ, ν and δ sufficiently small, there exists an $\epsilon_0 > 0$ so that the mapping $\tilde{z}_1 \mapsto \tilde{z}_{1,+}$ in (C.1) satisfies:*

$$\tilde{z}_{1,+}(\tilde{z}_1) = \mathcal{O}(\epsilon^{\frac{\mu\vartheta}{2}} (|\tilde{z}_1| + \ln \epsilon^{-1}) + \epsilon^{\frac{\vartheta}{2}}),$$

and

$$(\tilde{z}_{1,+})'(\tilde{z}_1) = \mathcal{O}(\epsilon^{\frac{\mu\vartheta}{2}}), \quad (\tilde{z}_{1,+})'(\tilde{z}_1)^{-1} = \mathcal{O}(\epsilon^{-\frac{\mu}{2\vartheta}}). \quad (\text{C.2})$$

for $\epsilon \leq \epsilon_0$.

Proof. To describe $\tilde{z}_{1,+}(\tilde{z}_1)$ we consider the initial conditions

$$r_1(0) = \rho, \quad \tilde{z}_1(0) = \tilde{z}_{10} \in I_1, \quad \epsilon_1(0) = \rho^{-2}\epsilon,$$

and let $T = \ln \left(\sqrt{\epsilon/(\rho^2\nu)} \right)^{-1}$ be so that

$$r_1(T) = \sqrt{\epsilon/\nu}, \quad \epsilon_1(T) = \nu.$$

Then $\tilde{z}_{1,+}(\tilde{z}_{10}) = \tilde{z}_1(T)$ and to estimate this we write the \tilde{z}_1 -equation as

$$\dot{\tilde{z}}_1 = -(\mu + \mathcal{O}(r_1 + \tilde{z}_1 + \epsilon_1)) \tilde{z}_1 + \mathcal{O}(r_1 + r_1 \epsilon_1),$$

introduce u by $u = e^{\mu t} \tilde{z}_1$, and then estimate $u(T)$ by Gronwall's integral inequality:

$$u(T) = (\tilde{z}_{10} + \mathcal{O}((\epsilon^{(1-\mu)/2} + 1) \ln \epsilon^{-1})) e^{\mathcal{O}(\rho+\delta+\nu)T}.$$

Here we have used the inequality

$$\int_0^t e^{(\mu-1)s} ds \leq (e^{(\mu-1)t} + 1)t,$$

for $t \geq 0$, to obtain a bound that is uniform in μ . Returning to \tilde{z}_1 we therefore obtain

$$\tilde{z}_1(T) = (\tilde{z}_{10} + \mathcal{O}(\ln \epsilon^{-1})) \epsilon^{\mu/2 + \mathcal{O}(\rho+\delta+\nu)} + \mathcal{O}(\epsilon^{1/2 + \mathcal{O}(\rho+\delta+\nu)}).$$

The estimates on $\partial_{\tilde{z}_{10}} \tilde{z}_{1,+} = \partial_{\tilde{z}_{10}} \tilde{z}_1(T)$ are similarly obtained by considering the variational equations. \square

By assumption (C) the set I_1 does not contain γ^w . Therefore the image of (C.1) described in Lemma C.1 is separated from γ_1^w at Λ_1^+ as follows:

LEMMA C.2. *Fix $\vartheta \in (0, 1)$. Then there exists a $K > 0$ so that*

$$K^{-1} \epsilon^{\frac{\mu}{2\vartheta}} \leq |\gamma_1^w \cap \Lambda_1^+ - (r_1, \hat{y}, \tilde{z}_1, \epsilon_1)| \leq K(\epsilon^{\frac{\mu\vartheta}{2}} + \epsilon^{\frac{\vartheta}{2}}), \quad (\text{C.3})$$

for any

$$(r_1, \hat{y}, \tilde{z}_1, \epsilon_1) = (\sqrt{\epsilon/\nu}, \hat{y}, \tilde{z}_1, \nu) \in I_1 \cap \Lambda_1^+,$$

and all ϵ sufficiently small.

As a corollary we have that the image of $\tilde{z}_{1,+}$ converges to

$$Q_1^1 \cap \Lambda_1^+,$$

as $\epsilon \rightarrow 0$.

C.2. Chart κ_3 . We now describe the set $I_3^t \cap \Lambda_3^+$ using the variables $(r_3, \tilde{y}, \hat{z}_3, \epsilon_3)$ in Lemma B.3.

LEMMA C.3. *For $K > 0$ sufficiently large, we have*

- *In case (i):*

$$I_3^t \cap \Lambda_3^+ \subset \{\Lambda_3^+ \mid 0 < K^{-1}\epsilon^{\frac{\mu}{2\vartheta}} \leq \tilde{y} \leq K(\epsilon^{\frac{\mu}{2}} + \epsilon^{\frac{\vartheta}{2}}), \quad |\hat{z}_3| \leq K(\epsilon^{\frac{\mu}{2}} + \epsilon^{\frac{\vartheta}{2}})\},$$

- *In case (ii):*

$$I_3^t \cap \Lambda_3^+ \subset \{\Lambda_3^- \mid -K(\epsilon^{\frac{\mu}{2}} + \epsilon^{\frac{\vartheta}{2}}) \leq \tilde{y} \leq -K^{-1}\epsilon^{\frac{\mu}{2\vartheta}} < 0, \quad |\hat{z}_3| \leq K(\epsilon^{\frac{\mu}{2}} + \epsilon^{\frac{\vartheta}{2}})\},$$

Proof. We work in chart κ_2 and apply the variational equations to describe the finite time flow map from Λ_2^- to Λ_2^+ for ϵ sufficiently small. The case when F is between $\gamma^w(0)$ and $\gamma^s(0)$ corresponds to variations in the positive direction of ϖ_{in} in (A.10). On the other hand, the case F between l^- and $\gamma^w(0)$ corresponds to variations in the negative direction of ϖ_{in} . Therefore, if we for example consider case (i), then the image vector ϖ_{out} , under the flow of the variational equations, is predominantly in the positive \hat{y} -direction (cf. (A.12)). This corresponds to positive values of \tilde{y} . The estimates (C.3) on the distance of the set $I_1 \cap \Lambda_1^-$ from the weak canard gives the desired result. \square

LEMMA C.4. *Fix $\vartheta \in (0, 1)$. Then for $\epsilon \ll 1$:*

- *In case (i): Then the mapping from $I_3^t \cap \Lambda_3^+$ to $\{\hat{y} = 1\}$ is well-defined with Jacobian $\mathcal{O}(\ln^{\frac{\mu}{2}} \epsilon^{-1})$ and image satisfying:*

$$I_3^t \cap \{\hat{y} = 1\} : (r_3, \tilde{z}_3, \epsilon_3) = (\mathcal{O}(\sqrt{\epsilon \ln \epsilon^{-1}}), \mathcal{O}(\ln^{-1} \epsilon^{-1}), \mathcal{O}(\ln^{-1} \epsilon^{-1})).$$

In particular $I_3^t \cap \{\hat{y} = 1\} \rightarrow (r_3, \tilde{z}_3, \epsilon_3) = 0$ for $\epsilon \rightarrow 0$.

- *In case (ii): Then the mapping from $I_3^t \cap \Lambda_3^+$ to $\{\hat{y} = -1\}$ is well-defined with Jacobian $\mathcal{O}(\ln^{\frac{\mu}{2}} \epsilon^{-1})$ and image satisfying:*

$$I_3^t \cap \{\hat{y} = -1\} : (r_3, \tilde{z}_3, \epsilon_3) = (\mathcal{O}(\sqrt{\epsilon \ln \epsilon^{-1}}), \mathcal{O}(\ln^{-1} \epsilon^{-1}), \mathcal{O}(\ln^{-1} \epsilon^{-1})).$$

In particular $I_3^t \cap \{\hat{y} = -1\} \rightarrow q_3^-$ for $\epsilon \rightarrow 0$ where

$$q_3^- : r_3 = 0, \hat{y} = -1, z_3 = -\chi_+, \epsilon_3 = 0.$$

Proof. We consider case (i) only. Case (ii) can be handled identically. Consider first the variables $(r_3, \tilde{y}, \hat{z}_3, \epsilon_3)$ of Lemma B.3 and consider the initial conditions

$$(r_3(0), \tilde{y}(0), \hat{z}_3(0), \epsilon_3) \in I_3^t \cap \Lambda_3^+.$$

as described in Lemma C.3. Let T be so that

$$\tilde{y}(T) = \nu, \tag{C.4}$$

We easily estimate T as

$$T = \mathcal{O}(\ln \epsilon^{-1}),$$

using (B.22). In the following we then quantify $r_3(T)$, $\hat{z}_3(T)$ and $\epsilon_3(T)$. Consider

$$\begin{aligned} r_3' &= r_3, \\ \hat{z}_3' &= (1 + \lambda_+^{-1} b \hat{z}_3)^{-1} (\mu - b \lambda_+^{-1} \hat{z}_3) \tilde{z}_3 + r_3 G_0(r_3, \hat{z}_3) + \epsilon_3 r_3 G_1(r_3, \epsilon_3) + \epsilon_3 \hat{z}_3 G_2(r_3, \hat{z}_3, \epsilon_3), \\ \epsilon_3' &= -2\epsilon_3. \end{aligned}$$

obtained from (B.20) by division of ϵ_3 . Denote the new time by \tilde{t} so that

$$d\tilde{t} = \epsilon_3 dt. \tag{C.5}$$

Using $\epsilon_3 = e^{-2\tilde{t}}\nu$ we obtain the transition time \tilde{T} with respect to time \tilde{t} as

$$\tilde{T} = \ln \sqrt{\tilde{T}}(1 + o(1)).$$

Therefore

$$r_3(T) = \mathcal{O}(\sqrt{\epsilon \ln \epsilon^{-1}}),$$

and

$$\epsilon_3(T) = \mathcal{O}(\ln^{-1} \epsilon^{-1}).$$

We can estimate $\tilde{z}_3(T)$ by using \hat{z}_3 in (B.19) and write the corresponding equation as

$$\dot{\hat{z}}_3 = (\mu + \mathcal{O}(r_3 + \hat{z}_3 + \epsilon_3))\hat{z}_3 + \mathcal{O}(r_3 + r_3\epsilon_3).$$

We obtain

$$\hat{z}_3(T) = \mathcal{O}(e^{\mu\vartheta\tilde{T}}|\hat{z}_{30}| + \sqrt{\epsilon}(\tilde{T}e^{\mu\vartheta\tilde{T}} + e^{\vartheta\tilde{T}})),$$

with $\vartheta \in (0, 1)$. We then return to \tilde{z}_3 and use the fact $\hat{z}_{30} = \mathcal{O}(\epsilon^{\frac{\mu\vartheta}{2}} + \epsilon^{\frac{\vartheta}{2}})$ for initial conditions in $I_3^t \cap \Lambda_3^+$, to obtain

$$\tilde{z}_3(T) = \mathcal{O}(\ln^{-1} \epsilon^{-1}).$$

In total:

$$(r_3(T), \tilde{z}_3(T), \epsilon_3(T)) = (\mathcal{O}(\sqrt{\epsilon \ln \epsilon^{-1}}), \mathcal{O}(\ln^{-1} \epsilon^{-1}), \mathcal{O}(\ln^{-1} \epsilon^{-1})), \quad (\text{C.6})$$

at $\tilde{y}(T) = \pm v$. By considering the variational equations we similarly obtain

$$\partial_{\tilde{z}_{30}} \tilde{z}_3(T) = \mathcal{O}(\ln^{\frac{\mu\vartheta}{2}} \epsilon^{-1}). \quad (\text{C.7})$$

Now to finish the description of the mapping we map (C.6) from $\tilde{y} = v$ to $\hat{y} = 1$. Note that $\dot{\hat{y}} \geq c(v)$ for $\tilde{y} \geq v$ for some $c(v) > 0$, for ϵ sufficiently small. The estimates for r_3 , \tilde{z}_3 and ϵ_3 in (C.6) and (C.7) do therefore not change by this $\mathcal{O}(1)$ -time flow-map application. \square

C.3. Case (ii). The fold line l^- is invisible and the set I^t in Lemma C.4 therefore revisits $\{\hat{y} = -1\}$ within chart κ_1 for $\epsilon \ll 1$. To describe this return we follow the direct approach outlined in Appendix A.7.1.

Let $X^- = (X_1^-, X_2^-, X_3^-)$ be the PWS vector-field in (2.6). Then we define the following curve of fold-points with $y = -\epsilon$:

$$l_\epsilon^- : \quad y = -\epsilon, \quad X_2^-(x, -\epsilon, z) = 0.$$

Using the explicit form of X_2^- in (2.6) we obtain the following:

$$l_\epsilon^- : \quad y = -\epsilon, \quad x = x_f(\epsilon, z) \equiv |\beta|^{-1}\alpha\epsilon + \mathcal{O}(\epsilon^2),$$

by applying the implicit function theorem. We then define the following mapping

$$\sigma_\epsilon^- : \{y = -\epsilon, x > x_f(\epsilon, z)\} \rightarrow \{y = -\epsilon, x < x_f(\epsilon, z)\},$$

through the forward flow of X^- . We will write this mapping in the coordinates of κ_1 and κ_3 and therefore consider:

$$\sigma_{13}^- = \kappa_1 \circ \sigma_\epsilon^- \circ \kappa_3^{-1} : (r_3, z_3, \epsilon_3) \mapsto (r_1, z_1, \epsilon_1).$$

We obtain the following proposition:

LEMMA C.5. *The mapping σ_{13}^- takes the following form:*

$$\begin{aligned}\sigma_{13}^- : \quad r_1 &= r_3(1 + \mathcal{O}(r_3)), \\ z_1 &= z_3 + \frac{2\gamma}{b} + \mathcal{O}(r_3), \\ \epsilon_1 &= \epsilon_3(1 + \mathcal{O}(r_3)),\end{aligned}$$

and is smooth as a function of (r_3, z_3, ϵ_3) , even for $r_3 = 0$.

Proof. This follows from Proposition 2.6 and the fact that $\sigma_\epsilon = \sigma_0 + \mathcal{O}(\epsilon) = \sigma_0 + \mathcal{O}(r_3^2 \epsilon_3)$. \square

From this lemma we then obtain:

LEMMA C.6. *The image of q_3^- (see (A.3)) under σ_{13}^- is given by*

$$q_1^- \equiv \sigma_{13}^-(q_3^-) : \quad r_1 = 0, \quad z_1 = z_1^*, \quad \epsilon_1 = 0, \quad (\text{C.8})$$

with z_1^* as in (2.20):

$$z_1^* = -\chi_+ + \frac{2\gamma}{b} > \chi_-. \quad (\text{C.9})$$

Proof. The image of σ_{13}^- is obtained by a direct calculation. \square

LEMMA C.7. *The set $I_1^t \cap \{\hat{y} = -1\}$ satisfies*

$$I_1^t \cap \{\hat{y} = -1\} : \quad r_1 = \mathcal{O}(\sqrt{\epsilon \ln \epsilon^{-1}}), \quad z_1 = z_1^* + \mathcal{O}(\ln^{-1} \epsilon^{-1}), \quad \epsilon_1 = \mathcal{O}(\ln^{-1} \epsilon^{-1}). \quad (\text{C.10})$$

The Jacobian of the assignment from $I_3^t \cap \{\hat{y} = -1\}$ to $I_1^t \cap \{\hat{y} = -1\}$ under σ_{13}^- is $I + \mathcal{O}(\ln^{-1} \epsilon)$.

Proof. The set $I_1^t \cap \{\hat{y} = -1\}$ is the image of the set $I_3^t \cap \{\hat{y} = -1\}$, described in Lemma C.4, under the mapping σ_{13}^- . Using Lemma C.5 the result then follows. \square

C.4. The case $z_1^* < 0$. The point $q_1^+ : r_1 = 0, \hat{y} = 1, z_1 = 0, \epsilon_1 = 0$ in (A.25) is a nonhyperbolic point of (B.1) so (in principle) a further blowup is required to study this region. This is due to the loss of hyperbolicity of \hat{l}^+ (see also Theorem 3.3).

To present the blowup of q_1^+ we first center \hat{y} about $\hat{y} = 1$ and recall Definition 3.1 and in particular that $\phi \in C^k$ with

$$1 \leq k < \infty,$$

so that by 3° in Definition 3.1

$$\phi(1 + \hat{y}) = 1 - \phi^{[n]}(-\hat{y})^n(1 + \mathcal{O}(\hat{y})), \quad \phi^{[n]} = \frac{(-1)^{n+1}}{n!} \phi^{(n)}(1) > 0,$$

for $\hat{y} \in [-2, 0]$. Here we have defined

$$n = k + 1.$$

Dropping the subscripts on (r_1, z_1, ϵ_1) we obtain the following system:

$$\begin{aligned}\dot{r} &= -r\epsilon, \\ \dot{\hat{y}} &= |\beta|c^{-1} \left(bz(1 + \mathcal{O}(r + \hat{y}^n)) + \frac{1}{2}|\beta|\phi^{[n]}(-\hat{y})^n(1 + \mathcal{O}(r + \hat{y})) \right), \\ \dot{z} &= \epsilon(2|\beta|c^{-1}(1 + \mathcal{O}(r + \hat{y}^n)) + z), \\ \dot{\epsilon} &= 2\epsilon^2,\end{aligned}$$

for $\hat{y} \leq 0$, after division by the non-zero function $G_1 = 2|\beta|^{-1}c(1 + \mathcal{O}(r))(1 + \mathcal{O}(\hat{y}^n))$. We will then apply the following blowup

$$z = \varrho^n \bar{z}, \quad \hat{y} = \varrho \bar{y}, \quad \epsilon = \varrho^{2n-1} \bar{\epsilon}, \quad (\varrho, (\bar{z}, \bar{y}, \bar{\epsilon})) \in \overline{\mathbb{R}}_+ \times S^2, \quad (\text{C.11})$$

considering only the southern hemisphere: $\bar{y} \leq 0$. We desingularize through division by $\varrho^{n-1} = \varrho^k$. The blowup (C.11) is similar to the blowup used in [15, Eqs. (6.4) and (6.9)] to study the regularization of the visible fold line \hat{l}^+ away from \hat{q} . We use the following two charts:

$$\begin{aligned}\kappa_{1,1} : \quad z &= -\varrho_1^n, \quad \hat{y} = \varrho_1 y_1, \quad \epsilon = \varrho_1^{2n-1} \epsilon_1, \\ \kappa_{2,1} : \quad z &= \varrho_2^n z_2, \quad \hat{y} = \varrho_2 y_2, \quad \epsilon = \varrho_2^{2n-1},\end{aligned}$$

to describe the blowup. In chart $\kappa_{1,1}$ the orbit Q_1^5 is denoted by $Q_{1,1}^5$. Similarly the point q_1^+ becomes $q_{1,1}^+$. We will need the following coordinate changes between $\kappa_{1,1}$ ($\kappa_{2,1}$) and $\kappa_{2,1}$ ($\kappa_{1,1}$):

$$z_2 = -\epsilon_1^{-n/(2n-1)}, \quad y_2 = y_1 \epsilon_1^{-1/(2n-1)}, \quad \varrho_2 = \varrho_1 \epsilon_1^{1/(2n-1)}, \quad (\text{C.12})$$

$$\epsilon_1 = (-z_2)^{-(2n-1)/n}, \quad y_1 = y_2 (-z_2)^{-1/n}, \quad \varrho_1 = \varrho_2 (-z_2)^{1/n}, \quad (\text{C.13})$$

defined for $\epsilon_1 > 0$ ($z_2 < 0$).

Chart $\kappa_{1,1}$. In this chart we obtain the following system of equations:

$$\begin{aligned}\dot{r} &= -\varrho_1^n \epsilon_1 r, \\ \dot{\varrho}_1 &= -\frac{1}{n} \varrho_1 \epsilon_1 H_1(r, \varrho_1, y_1, \epsilon_1), \\ \dot{y}_1 &= |\beta| c^{-1} \left(-b(1 + \mathcal{O}(r + \varrho_1^n)) + \frac{1}{2} |\beta| \phi^{[n]} (-y_1)^n (1 + \mathcal{O}(r + \varrho_1)) \right) + \frac{1}{n} \epsilon_1 y_1 H_1(r, \varrho_1, \hat{y}_1, \epsilon_1), \\ \dot{\epsilon}_1 &= \frac{2n-1}{n} \epsilon_1^2 H_1(r, \varrho_1, y_1, \epsilon_1) + 2\varrho_1^n \epsilon_1^2,\end{aligned}$$

after division by ϱ_1^{n-1} , where

$$H_1(r, \varrho_1, y_1, \epsilon_1) = 2|\beta| c^{-1} (1 + \mathcal{O}(r + \varrho_1^n)) > 0.$$

Within $r = \epsilon_1 = 0$ of chart $\kappa_{1,1}$ we re-discover Q_1^5 as a set of equilibria:

$$Q_{1,1}^5 : \quad r = 0, \quad \varrho_1 \geq 0, \quad y_1 = -\left(\frac{2b}{|\beta| \phi^{[n]}} \right)^{1/n} (1 + \mathcal{O}(\varrho_1)), \quad \epsilon_1 = 0. \quad (\text{C.14})$$

By the blowup (C.11) we gain hyperbolicity of the end of (C.14):

$$q_{1,1}^+ : \quad r = 0, \quad \varrho_1 \geq 0, \quad y_1 = -\left(\frac{2b}{|\beta| \phi^{[n]}} \right)^{1/n}, \quad \epsilon_1 = 0. \quad (\text{C.15})$$

Indeed the linearization about $q_{1,1}^+$ gives three zero eigenvalues and one single negative eigenvalue:

$$-\frac{n}{2} |\beta|^2 c^{-1} \phi^{[n]} \left(\frac{2b}{|\beta| \phi^{[n]}} \right)^{(n-1)/n}.$$

Therefore:

LEMMA C.8. *There exists an attracting center manifold*

$$N_{a,1} : \quad y_1 = m(r, \varrho_1, \epsilon_1) \equiv -\left(\frac{2b}{|\beta| \phi^{[n]}} \right)^{1/n} (1 + \mathcal{O}(\epsilon_1 + r + \varrho_1^n)),$$

for $\varrho_1 \leq \rho$ and $\epsilon_1 \leq \nu$ sufficiently small, containing (C.14) within $r = \epsilon_1 = 0$ and

$$r = 0, \quad \varrho_1 = 0, \quad y_1 = -\left(\frac{2b}{|\beta| \phi^{[n]}} \right)^{1/n} (1 + \mathcal{O}(\epsilon_1)), \quad \epsilon_1 \geq 0. \quad (\text{C.16})$$

as a unique invariant sub-manifold within $r = \varrho_1 = 0$.

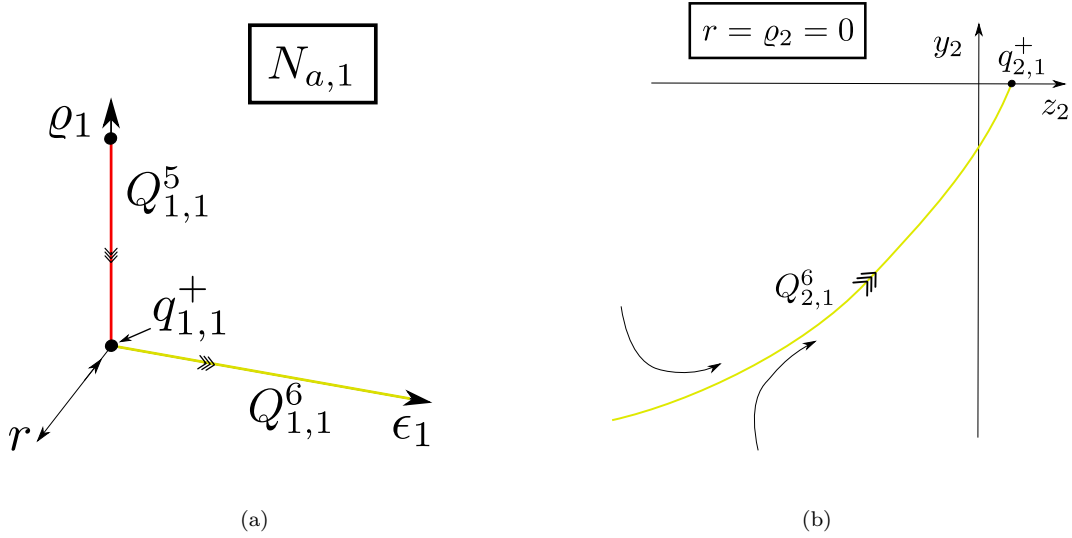


FIGURE C.1. (a): Illustration of $Q_{1,1}^5$, $q_{1,1}^+$, and $Q_{1,1}^6$ within $N_{a,1}$ in chart $\kappa_{1,1}$. (b): Illustration of $Q_{2,1}^6$

Proof. Straightforward. The center manifold in (C.16) is a unique since $\dot{\epsilon}_1 > 0$ for $\epsilon_1 > 0$. \square
 On $N_{a,1}$ we obtain the reduced problem

$$\begin{aligned} \dot{r} &= -\frac{1}{2}|\beta|^{-1}c\varrho_1^n(1 + \mathcal{O}(r + \varrho_1^n))r, \\ \dot{\varrho}_1 &= -\frac{1}{n}\varrho_1, \\ \dot{\epsilon}_1 &= \frac{2n-1}{n}(1 + \mathcal{O}(\varrho_1^n))\epsilon_1, \end{aligned} \quad (\text{C.17})$$

after further division by $\epsilon_1 H_1$. It suffices to consider the dynamics on $N_{a,1}$. Indeed, by the blowup we have uniform contraction along $N_{a,1}$. The origin is hyperbolic for (C.17) $_{r=0}$ and it corresponds to $q_{1,1}^+$. The orbit $Q_{1,1}^5 = \{\varrho_1 \geq 0, r = \epsilon_1 = 0\}$ is the strong stable manifold of $q_{1,1}^+$ for (C.17), while

$$Q_{1,1}^6 = \{\epsilon_1 \geq 0, r = \varrho_1 = 0\},$$

corresponding to (C.16), is the associated unstable manifold. We can therefore follow a neighborhood of the point

$$Q_{1,1}^5 \cap \{r_1 = \rho\}$$

to a neighborhood of the point

$$r = 0, \varrho_1 = 0, y_1 = -\left(\frac{2b}{|\beta|\phi^{[n]}}\right)^{1/n} (1 + \mathcal{O}(\nu)), \epsilon_1 = \nu, \quad (\text{C.18})$$

using $Q_{1,1}^{5,6}$ as guides. We skip the details.

We illustrate the reduced dynamics and the relevant objects in Fig. C.1 (a). We continue the point (C.18) by moving to chart $\kappa_{2,1}$. In this chart, the orbit segment $Q_{1,1}^6$ will be denoted by $Q_{2,1}^6$.

Chart $\kappa_{2,1}$. In this chart we obtain the following system:

$$\begin{aligned}\dot{r} &= -r\varrho_2^n, \\ \dot{\varrho}_2 &= \frac{2}{2n-1}\varrho_2^{n+1}, \\ \dot{y}_2 &= |\beta|c^{-1} \left(bz_2(1 + \mathcal{O}(r + \varrho_2^n)) + \frac{1}{2}|\beta|\phi^{[n]}(-y_2)^n(1 + \mathcal{O}(r + \varrho_2)) \right) - \frac{2}{2n-1}\varrho_2^n y_2, \\ \dot{z}_2 &= 2|\beta|c^{-1}(1 + \mathcal{O}(r + \varrho_2^n)),\end{aligned}$$

after division by ϱ_2^{n-1} . Consider $r = 0$, $\varrho_2 = 0$:

$$\begin{aligned}\dot{y}_2 &= bz_2 + \frac{1}{2}|\beta|\phi^{[n]}(-y_2)^n, \\ \dot{z}_2 &= 2,\end{aligned}$$

after a further change of time.

LEMMA C.9. *Let $n = k + 1$. Then the orbit $Q_{2,1}^6 \subset \{r = \varrho_2 = 0\}$ intersects $y_2 = 0$ in*

$$r = 0, \varrho_2 = 0, y_2 = 0, z_2 = c_z \eta(n),$$

where $\eta(n) > 0$ only depends on n (or simply $k = n - 1$) and

$$c_z = \left(\frac{2^{n+1}}{|\beta|b^{n-1}\phi^{[n]}} \right)^{1/(2n-1)}. \quad (\text{C.19})$$

Proof. Using (C.12) and (C.13) we obtain the following asymptotics for $z_2 \ll 0$ for the unique center manifold $Q_{2,1}^6$:

$$Q_{2,1}^6: \quad r = 0, \varrho_2 = 0, y_2 = - \left(\frac{2b}{|\beta|\phi^{[n]}} \right)^{1/n} (-z_2)^{1/n} (1 + \mathcal{O}((-z_2)^{-(2n-1)/n})). \quad (\text{C.20})$$

Let

$$y_2 = c_y u, \quad z_2 = c_z v,$$

with c_z as in (C.19) and

$$c_y = -\frac{b}{2}c_z^2.$$

Within $r = \varrho_2 = 0$ we then obtain the following system in (u, v) :

$$\begin{aligned}\dot{u} &= -v - u^n, \\ \dot{v} &= 1,\end{aligned}$$

after scaling time by $2c_z^{-1}$. The unique center manifold in (C.20) then becomes

$$u = (-v)^{1/n} (1 + \mathcal{O}((-v)^{-(2n-1)/n}))$$

for $v \ll 0$ in these variables. In [2, Proposition 3.10] this manifold is guided up until $v = 0$ (corresponding to $y_2 = 0$) where it intersects in a point

$$(u, v) = (0, \eta(n)),$$

with $\eta(n) > 0$. Returning to (z_2, y_2) we obtain the desired result. \square

An illustration is available in Fig. C.1 (b). By regular perturbation theory and the contraction in Lemma C.1 we obtain the desired properties of the mapping \mathcal{L}_ϵ in Proposition 5.5, proving the proposition in case (ii) for $z_1^* \in (\chi_-, 0)$.

C.5. The case $z_1^* > 0$. This case corresponds to the crossing region Σ_{cr}^+ . For ϵ sufficiently small the fast variable, \hat{y} , in (B.1) is therefore increasing for all initial conditions in $I_1^t \subset \{\hat{y} = -1\}$. In particular, the forward flow of the point q_1^- gets mapped to the point

$$r_1 = 0, \hat{y} = 1, z_1 = z_1^*, \epsilon_1 = 0,$$

by following a fast orbit segment. It is then straightforward to obtain the following:

LEMMA C.10. *initial conditions in $I_1^t \cap \{\hat{y} = -1\}$ gets mapped to a subset of $\{\hat{y} = 1\}$ with*

$$r_1 = \mathcal{O}(\sqrt{\epsilon \ln \epsilon^{-1}}), \quad z_1 = z_1^* + \mathcal{O}(\ln^{-1} \epsilon^{-1}), \quad \epsilon_1 = \mathcal{O}(\ln^{-1} \epsilon^{-1}).$$

The associated Jacobian is $I + \mathcal{O}(\ln^{-1} \epsilon^{-1})$.

C.6. Exceptional case: $z_1^* = 0$. The only case left to consider is the exceptional case where $z_1^* = 0$. First, we note that from $z_1, \epsilon_1 = \mathcal{O}(\ln^{-1} \epsilon^{-1})$ (by (C.10)) it follows that $z_2 = \mathcal{O}(\ln^{-(n-1)/(2n-1)} \epsilon^{-1})$ in chart $\kappa_{2,1}$. Therefore we can work in chart $\kappa_{2,1}$ (upon a simple passage through the chart $\bar{y} = -1$) of (C.11). Then using a phase plane analysis in the (y_2, z_2) -plane it can be established that the forward flow of $I_1^t \cap \{\hat{y} = -1\}$ intersects $\{y_2 = 0\}$ (corresponding to $\{\hat{y} = 1\}$) in a set with

$$r = \mathcal{O}(\sqrt{\epsilon \ln \epsilon^{-1}}), \quad \varrho_2 = \mathcal{O}(\ln^{-\frac{\nu}{2n-1}} \epsilon^{-1}),$$

and

$$c_z^{-1} z_2 \in (\eta(n) + K^{-1}, K),$$

with c_z as in (C.19) and $K = K(n)$ large enough. The Jacobian is $\mathcal{O}(1)$. Blowing and scaling back down then completes the proof Proposition 5.5.

Appendix D. Blowup of \hat{q} in chart $\bar{y} = -1$. In this section we consider the analysis of the charts $\kappa_{3,2,1}$ used to describe the blowup cylinder of (A.18) in the chart $\bar{y} = -1$ of (3.7).

D.1. Chart κ_3 . In this chart we obtain the following equations:

$$\begin{aligned} \dot{r}_3 &= -r_3 y_3 K_3(r_3, y_3, z_3, \hat{\epsilon}), \\ \dot{y}_3 &= y_3 (J_3(r_3, y_3, z_3, \hat{\epsilon}) + 2y_3 K_3(r_3, y_3, z_3, \hat{\epsilon})), \\ \dot{z}_3 &= -y_3 (b^{-1}\gamma + \mathcal{O}(r_3) - z_3 K_3(r_3, y_3, z_3, \hat{\epsilon})), \\ \dot{\hat{\epsilon}} &= -\hat{\epsilon} J_3(r_3, y_3, z_3, \hat{\epsilon}), \end{aligned} \tag{D.1}$$

for $y_3 \leq 0$, where

$$\begin{aligned} K_3(r_3, y_3, z_3, \hat{\epsilon}) &= -1 + \mathcal{O}(r_3), \\ J_3(r_3, y_3, z_3, \hat{\epsilon}) &= |\beta| + \mathcal{O}(r_3). \end{aligned}$$

The point q_3^- in (A.3) becomes

$$q_3^- : \quad r_3 = 0, y_3 = 0, z_3 = -\chi_+, \hat{\epsilon} = 1. \tag{D.2}$$

in this chart We will continue to denote this point by this symbol in this new chart. Furthermore, $Q_3^{2,-}$ in (A.4) for $\hat{y} < 0$ becomes

$$Q_3^{2,-} : \quad r_3 = y_3 = 0, z_3 = -\chi_-, \hat{\epsilon} \geq 0.$$

We continue to use the same symbol. $Q_3^{2,-}$ is invariant for (D.1) and in particular the forward flow takes (D.2) to the point

$$r_3 = 0, y_3 = 0, \epsilon_3 = 0, z_3 = -\chi_+. \tag{D.3}$$

Linearizing (D.1) about (D.3) gives a semi-simple matrix with eigenvalues

$$\pm|\beta|, 0, 0, \tag{D.4}$$

and associated eigenvectors

$$(0, -|\beta|, b^{-1}\gamma - \chi_+, 0), (0, 0, 0, 1), (1, 0, 0, 0), (0, 0, 1, 0).$$

We have

LEMMA D.1. *There exists a 1D unstable manifold of (D.3) of the following form:*

$$Q_3^3 : \quad y_3 = \frac{1}{2}|\beta| \left(1 - \left(\frac{b^{-1}\gamma + z_3}{b^{-1}\gamma - \chi_+} \right)^2 \right), r_3 = \hat{\epsilon} = 0, z_3 \geq -\chi_+. \tag{D.5}$$

Furthermore, the set $Q_3^{2,-}$ is a stable manifold of (D.3).

Proof. The existence of an unstable manifold follow from the positive eigenvalue $|\beta|$ in (D.4). The expression (D.5) is obtained by dividing (D.1) $_{r_3=\hat{\epsilon}=0}$ by $-y_3 \geq 0$ (corresponding to the introduction of a new time t_3) and then solving the corresponding system with the initial conditions corresponding to (D.3). This gives

$$\begin{aligned} y_3 &= \frac{1}{2}|\beta| (1 - e^{2t_3}), \\ z_3 &= -b^{-1}\gamma + (b^{-1}\gamma - \chi_+)e^{t_3}. \end{aligned} \tag{D.6}$$

Eliminating t_3 gives the desired expression for y_3 in (D.5).

The last statement about $Q_3^{2,-}$ is trivial. \square

The unstable manifold Q_3^3 brings us to chart κ_2 , where using the parametrization in (D.6), it becomes

$$\begin{aligned} x_2 &= \sqrt{\frac{2}{|\beta|}} (e^{2t_3} - 1)^{-1/2}, \\ z_2 &= \sqrt{\frac{2}{|\beta|}} (e^{2t_3} - 1)^{-1/2} (-b^{-1}\gamma + (b^{-1}\gamma - \chi_+)e^{t_3}), \\ r_2 &= 0, \quad \hat{\epsilon} = 0, \end{aligned} \tag{D.7}$$

using $x_2 = 1/(-y_3)^{-1/2}$, $z_2 = x_2 z_3$, and eventually, by the forward flow in chart κ_2 , into chart κ_1 . We skip the details of κ_2 and just notice that (D.7) satisfies:

$$x_2 \rightarrow 0, \quad z_2 \rightarrow (b^{-1}\gamma - \chi_+) \sqrt{\frac{2}{|\beta|}}, \tag{D.8}$$

for $t_3 \rightarrow \infty$. We consider chart κ_1 in the following.

D.2. Chart κ_1 . In this chart we obtain the following equations:

$$\begin{aligned} \dot{r}_1 &= r_1 y_1 K_1(r_1, y_1, z_1, \hat{\epsilon}), \\ \dot{y}_1 &= -y_1 (J_1(r_1, y_1, z_1, \hat{\epsilon}) + 2y_1 K_1(r_1, y_1, z_1, \hat{\epsilon})), \\ \dot{z}_1 &= -y_1 (b^{-1}\gamma + \mathcal{O}(r_1) + z_3 K_1(r_1, y_1, z_1, \hat{\epsilon})), \\ \dot{\hat{\epsilon}} &= \hat{\epsilon} J_1(r_1, y_1, z_1, \hat{\epsilon}), \end{aligned} \tag{D.9}$$

for $y_1 \leq 0$, where

$$\begin{aligned} K_1(r_1, y_1, z_1, \hat{\epsilon}) &= -1 + \mathcal{O}(r_1), \\ J_1(r_1, y_1, z_1, \hat{\epsilon}) &= |\beta| + \mathcal{O}(r_1). \end{aligned}$$

The line $r_1 = y_1 = \hat{\epsilon} = 0$, $z_1 \geq \mathbb{R}$ is a line of fix point of (D.9). The linearization about the point

$$(r_1, y_1, z_1, \hat{\epsilon}) = (0, 0, z_1^*, 0), \tag{D.10}$$

gives a semi-simple matrix with eigenvalues

$$-|\beta|, |\beta|, 0, 0,$$

and associated eigenvectors

$$(0, |\beta|, b^{-1}\gamma - z_1, 0), (0, 0, 0, 1), (1, 0, 0, 0), (0, 0, 1, 0).$$

LEMMA D.2. *There exists a 1D stable manifold of (D.10) of the following form*

$$Q_1^3: \quad y_1 = \frac{1}{2}|\beta| \left(1 - \left(\frac{b^{-1}\gamma - z_1}{b^{-1}\gamma - z_1^*} \right)^2 \right) \leq 0, \quad r_1 = \hat{\epsilon} = 0.$$

Proof. Within $r_1 = \hat{\epsilon} = 0$ we obtain the following expression for the stable manifold associated with the fix-point at $(y_1, z_1) = (0, z_1^*)$:

$$\begin{aligned} y_1 &= \frac{|\beta|}{2} (1 - e^{-2t_1}), \\ z_1 &= b^{-1}\gamma + (z_1^* - b^{-1}\gamma) e^{-t_1}, \end{aligned} \tag{D.11}$$

for $t_1 \leq 0$, by dividing (D.9) _{$r_1=\hat{\epsilon}=0$} by $-y_1$. Eliminating time t_1 gives the desired result. \square

Transforming (D.11) into chart κ_2 we obtain

$$x_2 \rightarrow 0, \quad z_2 \rightarrow (z_1^* - b^{-1}) \sqrt{\frac{2}{|\beta|}},$$

for $t_1 \rightarrow -\infty$. Setting this limit equal to the limit in (D.8) we obtain

$$z_1^* = -\chi_+ + \frac{2\gamma}{b}, \tag{D.12}$$

in agreement with (A.14), and we therefore conclude that the forward flow of the unstable manifold Q_3^3 in Lemma D.1 obtained in chart κ_3 coincides with the stable manifold Q_1^3 obtained in Lemma D.2 with z_1^* as in (D.12). The heteroclinic connection \bar{Q}^3 obtained in this way consists of points that are backward asymptotic to (D.3) in chart κ_3 and forward asymptotic to (D.10) in chart κ_1 .

LEMMA D.3. *There exists a 1D unstable manifold of (D.10) of the following form*

$$Q_1^4 : \quad r_1 = y_1 = 0, \quad z_1 = z_1^*, \quad \hat{\epsilon} \geq 0.$$

Proof. Straightforward calculation. \square

Following Q_1^4 , we reach the point q_1^- in (C.8), which in this chart becomes

$$q_1^- : \quad r_1 = 0, \quad y_1 = 0, \quad z_1 = z_1^*, \quad \hat{\epsilon} = 1.$$

This gives the picture of the singular orbit composed of three parts: $\bar{Q}^{2,-}$, \bar{Q}^3 and \bar{Q}^4 which is illustrated in Fig. A.3.

REFERENCES

- [1] E. Benoît, J. L. Callot, F. Diener, and M. Diener. Chasse au canard. *Collect. Math.*, 31-32:37–119, 1981.
- [2] C. Bonet-Reves and T. M-Seara. Regularization of sliding global bifurcations derived from the local fold singularity of filippov systems. *Discrete and Continuous Dynamical Systems*, 36(7):3545–3601, 2016.
- [3] E. Bossolini, M. Brøns, and K. Uldall Kristiansen. Singular limit analysis of a model for earthquake faulting. *arXiv:1603.02448 v2 [math.DS]*, 2016.
- [4] M. Brøns, M. Krupa, and M. Wechselberger. Mixed mode oscillations due to the generalized canard phenomenon. In W. Nagata and N. Sri Namachchivaya, editors, *Bifurcation Theory and Spatio-Temporal Pattern Formation*, volume 49 of *Fields Institute Communications*, pages 39–64. American Mathematical Society, 2006.
- [5] A. Colombo and M. R. Jeffrey. Nondeterministic chaos, and the two-fold singularity in piecewise smooth flows. *SIAM Journal on Applied Dynamical Systems*, 10(2):423–451, 2011.
- [6] J. Cortez. Discontinuous dynamical systems. *Control Systems, IEEE*, 28(3):36–73, 2008.
- [7] M. Desroches and M. R. Jeffrey. Canards and curvature: nonsmooth approximation by pinching. *Nonlinearity*, 24(5):1655–1682, May 2011.
- [8] N. Fenichel. Persistence and smoothness of invariant manifolds for flows. *Indiana University Mathematics Journal*, 21:193–226, 1971.
- [9] N. Fenichel. Asymptotic stability with rate conditions. *Indiana University Mathematics Journal*, 23:1109–1137, 1974.
- [10] N. Fenichel. Geometric singular perturbation theory for ordinary differential equations. *J. Diff. Eq.*, 31:53–98, 1979.
- [11] A.F. Filippov. *Differential Equations with Discontinuous Righthand Sides*. Mathematics and its Applications. Kluwer Academic Publishers, 1988.
- [12] M. R. Jeffrey and S. J. Hogan. The geometry of generic sliding bifurcations. *SIAM Review*, 53(3):505–525, January 2011.
- [13] C.K.R.T. Jones. *Geometric Singular Perturbation Theory, Lecture Notes in Mathematics, Dynamical Systems (Montecatini Terme)*. Springer, Berlin, 1995.
- [14] K. Uldall Kristiansen. Blowup for flat slow manifolds with applications to regularization of piecewise smooth systems using tanh and a model of aircraft ground dynamics. *arXiv 1603:01821 [math.DS]*, 2016.
- [15] K. Uldall Kristiansen and S. J. Hogan. On the use of blowup to study regularizations of singularities of piecewise smooth dynamical systems in \mathbb{R}^3 . *SIAM Journal on Applied Dynamical Systems*, 14(1):382–422, 2015.
- [16] K. Uldall Kristiansen and S. J. Hogan. Regularizations of two-fold bifurcations in planar piecewise smooth systems using blowup. *SIAM Journal on Applied Dynamical Systems*, 14(4):1731–1786, 2015.
- [17] M. Krupa and P. Szmolyan. Extending geometric singular perturbation theory to nonhyperbolic points - fold and canard points in two dimensions. *SIAM Journal on Mathematical Analysis*, 33(2):286–314, 2001.
- [18] M. Krupa and P. Szmolyan. Relaxation oscillation and canard explosion. *Journal of Differential Equations*, 174(2):312–368, 2001.
- [19] C. Kuehn. *Multiple Time Scale Dynamics*. Applied Mathematical Sciences. Springer International Publishing, 2015.
- [20] O. Makarenkov and J. S. W. Lamb. Dynamics and bifurcation of nonsmooth systems: A survey. *Physica D*, 241:1826–1844, 2012.
- [21] D. J. W. Simpson. On resolving singularities of piecewise-smooth discontinuous vector fields via small perturbations. *Discrete and Continuous Dynamical Systems*, 34(10):3803–3830, 2014.
- [22] J. Sotomayor and M. A. Teixeira. Regularization of discontinuous vector fields. In *Proceedings of the International Conference on Differential Equations, Lisboa*, pages 207–223, 1996.
- [23] P. Szmolyan and M. Wechselberger. Canards in \mathbb{R}^3 . *J. Diff. Eq.*, 177(2):419–453, December 2001.
- [24] T. Vo, R. Bertram, and M. Wechselberger. Bifurcations of canard-induced mixed mode oscillations in a pituitary lactotroph model. *Discrete and Continuous Dynamical Systems*, 32(8):2879–2912, 2012.
- [25] M. Wechselberger. Existence and bifurcation of canards in \mathbb{R}^3 in the case of a folded node. *SIAM Journal on Applied Dynamical Systems*, 4(1):101–139, January 2005.